Solid Earth, 13, 1003–1026, 2022
https://doi.org/10.5194/se-13-1003-2022

Solid Earth Open Access EGU

Reconstructing post-Jurassic overburden in central Europe: new insights from mudstone compaction and thermal history analyses of the Franconian Alb, SE Germany

Simon Freitag[1], **Michael Drews**[2], **Wolfgang Bauer**[1], **Florian Duschl**[2], **David Misch**[3], **and Harald Stollhofen**[1]

[1]GeoZentrum Nordbayern, Friedrich-Alexander University (FAU) Erlangen–Nürnberg, Schlossgarten 5, 91054 Erlangen, Germany
[2]Geothermal Technologies, Technical University of Munich (TUM), Arcisstraße 21, 80333 Munich, Germany
[3]Department für Angewandte Geowissenschaften und Geophysik, Montanuniversität Leoben, Peter-Tunner-Straße 5, 8700 Leoben, Austria

Correspondence: Simon Freitag (simon.s.freitag@fau.de)

Received: 4 February 2022 – Discussion started: 15 February 2022
Revised: 12 May 2022 – Accepted: 25 May 2022 – Published: 21 June 2022

Abstract. The Franconian Alb of SE Germany is characterized by large-scale exposures of Jurassic shallow marine limestones and dolostones, which are frequently considered to be outcrop analogues for deep geothermal reservoir rocks in the North Alpine Foreland Basin farther south. However, the burial history of the Franconian Alb Jurassic strata is not well known as they were affected by emersion, leading to extensive erosion and karstification with only remnants of the original Cretaceous and Cenozoic cover rocks preserved. To estimate the original thicknesses of the post-Jurassic overburden we investigated the petrophysical properties and the thermal history of Lower and Middle Jurassic mudstones to constrain their burial history in the Franconian Alb area. We measured mudstone porosities, densities, and maturities of organic material and collected interval velocities from seismic refraction and logging data in shallow mudstone-rich strata. Mudstone porosities and P-wave velocities vertical to bedding were then related to a normal compaction trend that was calibrated on stratigraphic equivalent units in the North Alpine Foreland Basin. Our results suggest maximum burial depths of 900–1700 m, 300–1100 m of which is attributed to Cretaceous and younger sedimentary rocks overlying the Franconian Alb Jurassic units. Compared to previous considerations this implies a more widespread distribution and increased thicknesses of up to ∼ 900 m for Cretaceous and up to ∼ 200 m for Cenozoic units in SE Germany. Maximum overburden is critical to understand mechanical and diagenetical compaction of the dolostones and limestones of the Upper Jurassic of the Franconian Alb. The results of this study therefore help to better correlate the deep geothermal reservoir properties of the Upper Jurassic from outcrop to reservoir conditions below the North Alpine Foreland Basin. Here, the Upper Jurassic geothermal reservoir can be found at depths of up to 5000 m.

1 Introduction

1.1 Paleogeographic framework

The Franconian Alb east, south, and north of the city of Nuremberg (Fig. 1) is well known for its impressive exposures of Jurassic carbonates and reef structures in an area extending for ∼ 120 km east–west and ∼ 160 km north–south. The area is partly underlain by older structures such as the SW–NE-trending Carboniferous–Permian Kraichgau Basin (Lützner and Kowalczyk, 2012) and the upper Permian–Triassic Franconian Basin as part of the Germanic Basin (Freudenberger et al., 2013). Following dominantly terrestrial deposition during the Upper Triassic Keuper, marine environments returned during the Early Jurassic (Liassic), when the southern Germanic Basin was flooded, depositing mostly clays and clayey marls (Fig. 2) (Piénkowski et al., 2008). Alternating dark clays and oolitic ironstones

then record the Middle Jurassic (Dogger) (Piénkowski et al., 2008). With progressive shallowing of the epicontinental sea during the Late Jurassic (Malm), massive limestone and marlstone units, including siliceous sponge–microbial reefs and oolite platforms, formed (Koch and Munnecke, 2016; Meyer and Schmidt-Kaler, 1990; Piénkowski et al., 2008).

The Early Cretaceous was characterized by uplift contemporaneous with an overall marine regression, leading to pronounced erosion and karstification of the Franconian Alb Jurassic under tropical to subtropical climates (Schröder, 1968; Voigt et al., 2007). Uplift of the Bohemian Massif likely amounted up to $\sim$ 1–1.5 km (Peterek et al., 1996; Peterek and Schröder, 2010; Reicherter et al., 2008; Schröder, 1987; Wagner et al., 1997), probably related to far-field compression (Scheck-Wenderoth et al., 2008) and a wrench-dominated tectonic regime at the southern end of the North Sea rift system (Pharaoh et al., 2010). The uplifted basement areas of the Bohemian Massif and their eroded sedimentary cover sourced the coarse clastic–terrestrial Schutzfeldschichten (Lower Cretaceous), which likely covered the entire Franconian Alb (Freudenberger and Schwerd, 1996). Only in the course of several major northward marine transgressions during the Upper Cretaceous did the Franconian Alb area become flooded and successively buried by a thick pile of mixed siliciclastic and calcareous sediments. The initial collision between the African and the European plate during the Late Cretaceous then led to widespread inversion tectonics (Kley and Voigt, 2008; Scheck-Wenderoth et al., 2008; Voigt et al., 2008, 2021), resulting in basement uplift, the reactivation of faults such as the Franconian Line (Scheck-Wenderoth et al., 2008; Ziegler, 1989) (Fig. 1), and the removal of the majority of Cretaceous sediments (Schröder, 1987). A likely second major uplift phase was induced by the Alpine continental collision between the latest Late Cretaceous and Paleocene (Peterek et al., 1997; Reicherter et al., 2008; Schröder, 1987; Wagner et al., 1997; Ziegler, 1987). This, together with mantle-induced (upwelling asthenosphere) domal uplift below the Upper Rhine Graben Rift to the west of the Franconian Alb area (Fig. 1), caused southward tilting of the Mesozoic strata (von Eynatten et al., 2021). Subsequent and tilting-related differential erosion in turn resulted in the characteristic scarpland morphology (Schröder, 1968), leaving only local erosional remnants and residual weathering products (e.g., Kallmünz boulders, Alblehm) witnessing former Cretaceous overburden (Glaser et al., 2001; Schirmer, 2015).

Following long-lasting denudation, Cenozoic subsidence of the North Alpine Foreland Basin towards the south, contemporaneous with ongoing uplift of basement areas towards the east, led to erosional retreat of incised valleys that accommodated fluvial clastics during periods of base-level rise in the southern Franconian Alb area (Jin et al., 1995; Meyer, 1996; Zweigel et al., 1998). Nevertheless, the post-Jurassic burial history of the Franconian Alb area is rather uncertain, as only a few remnants of Cretaceous and Cenozoic sediments are preserved locally (Dill, 1995; Peterek et al., 1997; Peterek and Schröder, 2010).

1.2 Regional post-Jurassic thicknesses

Rather complete records of Cretaceous and Cenozoic sediments are only available within and below the central and eastern parts of the Cenozoic North Alpine Foreland Basin (Fig. 1; NAFB) in SE Germany and upper Austria. There, seismic- and borehole-data-based thicknesses of up to 900 m (Przybycin et al., 2015) or even up to 1000 m of Cretaceous (Meyer, 1996) and up to 5000 m of Cenozoic sediments are reported (Bachmann and Müller, 1992). Cenomanian to Campanian sediments are also preserved in the subsurface of the Braunau–Regensburg (BRB) and the Wasserburg basins (WB) (Fig. 3), which were both incorporated in the North Alpine Foreland Basin during the Alpine Orogeny and crop out only in the area of Regensburg (Voigt et al., 2008). Low-temperature thermochronology points to a good compliance between Late Cretaceous sediments at the marginal parts to the south of the Bohemian Massif, accompanied by continued uplift of the Variscan basement to the north, and subsequent exhumation and partial sediment removal since the Late Cretaceous and early Paleogene (Vamvaka et al., 2014). The Franconian Alb area directly north of the North Alpine Foreland Basin, however, had a different post-Jurassic and in particular post-Cretaceous burial history with the line Ingolstadt–Regensburg (Fig. 1) roughly dividing areas of Cenozoic subsidence versus non-subsidence and/or uplift. Towards the north, remnants of Cretaceous strata are only present on the eastern flank of the Franconian Alb close to distinct structural features such as the Danube Fault (DF), the Pfahl Fault (PF), and particularly the Franconian Line (Fig. 1) (Meyer, 1996; Schröder, 1987; Schröder et al., 1997), which are prominent NW–SE-striking, steeply NE-dipping upthrust faults that were repeatedly reactivated since the Permo-Triassic and superimposed basement rocks onto the Permo-Mesozoic sediment cover (Schröder, 1987; Zulauf, 1993). Nevertheless, the areal extent of sediment overburden since the Cretaceous still remains unclear (Eberle et al., 2017; Niebuhr et al., 2009), and only a few studies (Peterek and Schröder, 2010; Schröder, 1970, 1987) considered the burial history of the Franconian Alb and the original thicknesses of post-Jurassic sediments.

Based on geological field observations, Schröder (1970, 1987) estimated an original thickness of $>$ 300 m of Cretaceous sediments in the Franconian Alb area, a value which was later confirmed by Meyer (1996) and Peterek and Schröder (2010) based on paleogeographic considerations. From other published data a rough picture emerges of a Cretaceous sediment cover decreasing from $\sim$ 1–2 km (Hejl et al., 1997; Schröder, 1987) directly in front of the Franconian Line down to about 200–400 m farther west (Meyer, 1996; Niebuhr et al., 2009; Peterek and Schröder, 2010; Schröder, 1970; Voigt et al., 2008), eventually leading to total pinch-out

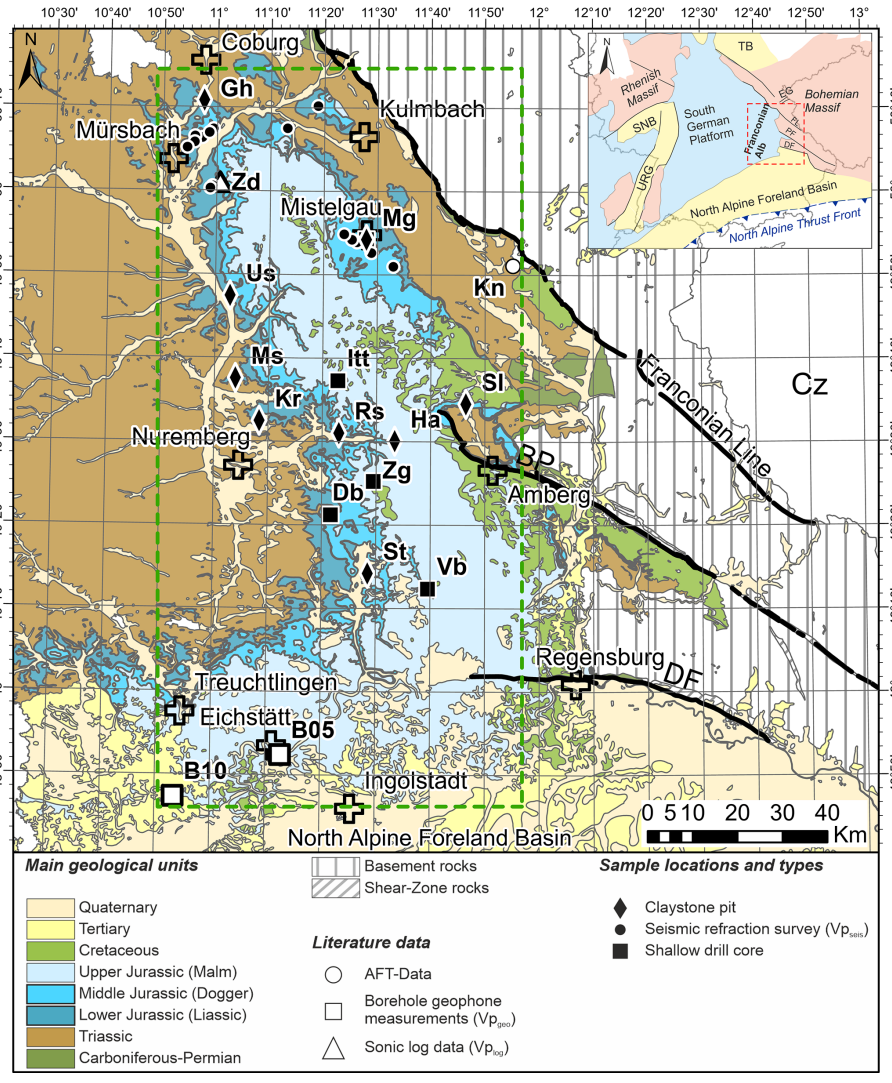

Figure 1. Geological map, including sample locations and sample types in the Franconian Alb area (green dashed box) with sampling focused on the Lower and Middle Jurassic units (dark blue fill). Abbreviations for claystone sample locations: Großheirath (Gh), Hartmannshof (Ha), Kalchreuth (Kr), Mistelgau (Mg), Marloffstein (Ms), Reichenschwand (Rs), Schönlind (Sl), Sengenthal (St), Unterstürmig (Us). Abbreviations for seismic refraction data and positions of shallow drill cores: Dörlbach (Db), Ittling (Itt), Mistelgau (Mg), Velburg (Vb), Zankschlag (Zg). Locations of samples used in AFT studies (white circle, Hejl et al., 1997) are Kemnath (Kn), seismic borehole data (white squares) are from Eichstätt (B05) and Daiting (B10) (Buness and Bram, 2001; Welz, 1994), and sonic log data are from Zapfendorf (Zd) (white triangle; Welz, 1994). Cz: Czech Republic. The inset at the upper right shows the location of the study area (red dashed box) in SE Germany and of relevant geological units in neighboring areas (PF: Pfahl Fault, DF: Danube Fault, EG: Eger Graben, SNB: Saar–Nahe Basin, TB: Thuringian Basin, URG: Upper Rhine Graben). Background data source: Bayerisches Landesamt für Umwelt, https://www.lfu.bayern.de/index.htm (last access: 17 January 2017).

towards the west to southwest (Peterek and Schröder, 2010). Hejl et al. (1997) used apatite fission-track (AFT) analysis to determine the low-temperature history of ortho- and paragneiss boulders that are situated to the east of the Franconian Alb, close to the Franconian Line. They infer a burial of up to 2000 m for Upper Cretaceous clastics in the proximal southwestern vicinity of the Franconian Line. Another more comprehensive AFT and (U−Th)/He analysis-based thermochronological study by von Eynatten et al. (2021) on the exhumation history of central Germany, including the Franconian Platform, points to large areas of Late Cretaceous to Paleocene domal uplift that experienced removal of 3–4 km of Mesozoic strata. In contrast, average vitrinite reflectance data for 0.7 %–0.8 % for lower Keuper (Ladinian) sediments just west of the northern Franconian Alb area constrain a much lower burial depth of 1.4 km (Bachmann et al., 2002). Subtracting reported regional middle–upper Keuper and Jurassic sediment thicknesses of 900 m in the southern

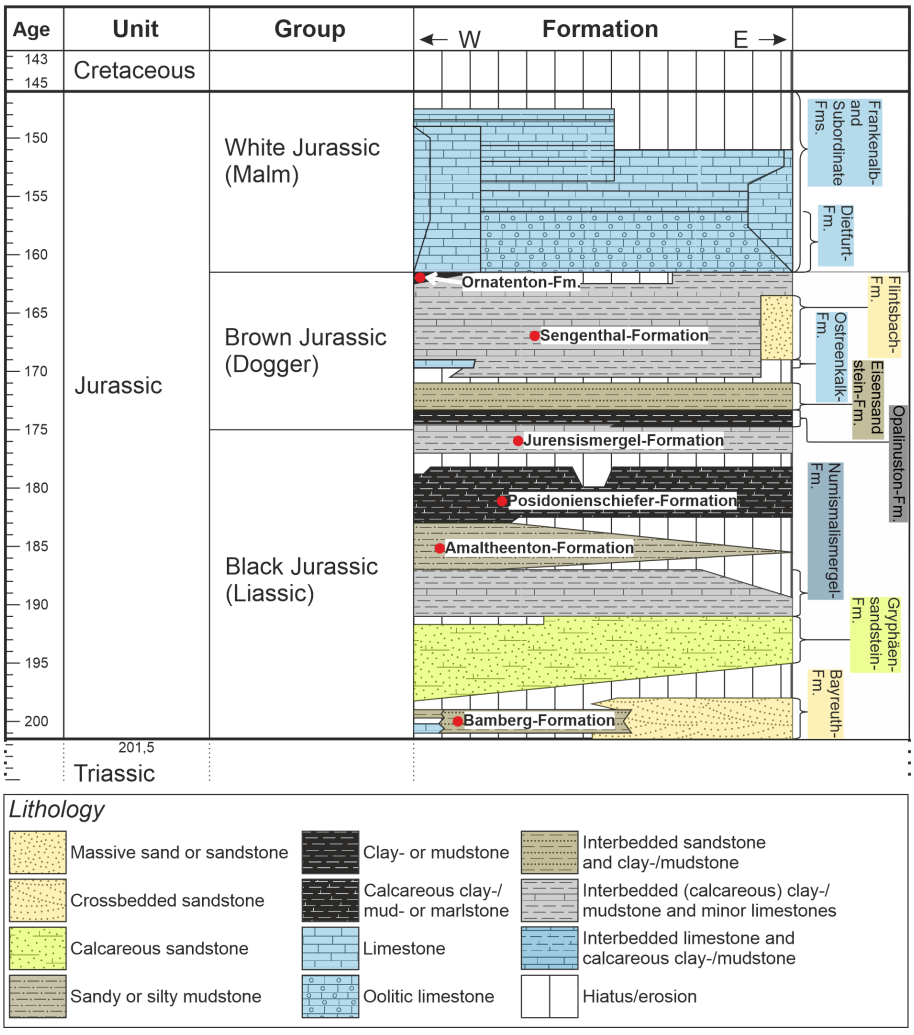

Figure 2. Jurassic stratigraphy of the Franconian Alb area with the stratigraphic positions of the samples marked by red dots (modified after German Stratigraphic Commission, 2016).

and 1400 m in the northern Franconian Alb area (Freudenberger and Schwerd, 1996) would suggest that no or only a < 500 m thick post-Jurassic sediment cover existed. As all of these studies did not quantify the maximum post-Jurassic sediment overburden, we aim to tackle this question by combining several methodological approaches that rely on independent datasets.

1.3 Study aim

In this study, we combine mudstone porosity and density data from helium and mercury porosimetry with vitrinite reflectance data and mudstone velocity data from downhole sonic velocity, downhole geophone, and seismic refraction field surveys to gain independent insights on the maximum burial of the Franconian Alb. The results will be compared with and discussed in the context of previous studies (Bader, 2001; Hejl et al., 1997; Peterek and Schröder, 2010; Schröder, 1987; von Eynatten et al., 2021).

Our results shed new light on the evolution of the Franconian Alb area and the original distribution and thicknesses of Cretaceous and Cenozoic sediments in central Europe. They are also of great relevance for an improved understanding of diagenetic pathways and hydraulic properties of the Permo-Triassic clastics and Late Jurassic carbonate rocks in the Franconian Alb. The latter serve as an important outcrop analogue for the most important deep geothermal (Malm) aquifer in the North Alpine Foreland Basin (Kröner et al., 2017; Mraz et al., 2018), whose petrophysical properties are known to strongly depend on burial depth (Bohnsack et al., 2020, 2021; Homuth et al., 2014; Steiner et al., 2014). Finally, the integration of different parameters and measurement types provides an important reference dataset (Table A2) for future studies, aiming to use petrophysical

properties of exhumed and near-surface located mudstones for burial history studies.

2 Data

2.1 Franconian Alb sample locations and data sources

We collected Lower (Liassic) and Middle Jurassic (Dogger) claystone and mudstone samples (Fig. 2) across the Franconian Alb area along a N–S transect from Coburg to Eichstätt and from Treuchtlingen to Amberg in the east–west direction (Fig. 1). Table 1 summarizes all sample locations, sample sources, sample types, sample depth below ground, and stratigraphic positions in addition to applied methods and number of measurements per sample.

Measured and calculated values for each sample are shown in Table A1 in the Appendix. Macroscopically "pure" Jurassic claystones and mudstones (minimum sample size $10 \times 10 \times 10$ cm) were selectively sampled at 0.5 m minimum depth (to avoid alteration and/or weathering) from nine active and closed claystone pits and from five newly drilled shallow drill cores (up to 12 m below ground level). Except for core samples from Velburg and Zankschlag all samples were packed and stored in an air-evacuated light-proof, waterproof, and air-proof aluminum barrier foil directly after extraction to preserve the best possible in situ conditions. Interval velocity data from Lias and Dogger claystones and mudstones from a shallow seismic refraction survey for low-velocity layers in the course of this study (see Fig. 1 for locations), published borehole geophone data from Buness and Bram (2001), and sonic log velocity data from a shallow wellbore (Zapfendorf) in the NW part of the study area (Welz, 1994) were also integrated.

2.2 Reference data from the North Alpine Foreland Basin

Density and sonic log data from nine deep wells in the North Alpine Foreland Basin (Fig. 3) have been filtered for appropriate mudstone intervals using gamma-ray (mudstone cutoff at 60–120 API) and/or resistivity values (mudstone cutoff at 4–8 Ωm) as a mudstone discriminator, and log values were subsequently averaged over 150 m depth intervals. The data were used to validate the normal compaction trend (NCT) determined by Drews et al. (2018) with regard to mudstone density data.

3 Methods

The degree of compaction has a strong influence on the mudstones' petrophysical properties, such as sonic velocity, density, and porosity (e.g., Bjørlykke, 1999; Giles et al., 1998; Mondol et al., 2008; Yang and Aplin, 2004). Mudstone compaction has been intensively studied in the past (e.g., Aplin et

Table 1. List of sample locations, sources, types, mean true vertical depth (TVD), stratigraphic unit, applied methods, and number of measurements per sample location (equal to the number of samples at the particular location). See Fig. 1 for sample locations and Fig. 2 for stratigraphic overview.

Location	Source	Type	Mean TVD (m)	Stratigraphic unit	GSC	ρ_t	$\rho_b/\emptyset_{Hg}$	v_P	VR	XRD
Daiting (B10)	Buness and Bram (2001)	Borehole geophone	455.0	Dogger				1		
Dörlbach (Db)	This study	Core	6.7	Posidonienschiefer Fm.		6	6		2	20
Eichstätt (B05)	Buness and Bram (2001)	Borehole geophone	327.0	Dogger				1		
Großheirath (Gh)	This study	Claystone pit	0.5	Bamberg Fm.	2	2	2		1	
Hartmannshof (Ha)	This study	Claystone pit	0.5	Sengenthal Fm.	1	1	1		2	1
Ittling (Itt)	This study	Core	20.7	Ornatenton		4	4			5
Kalchreuth (Kr)	This study	Claystone pit	0.0	Amaltheenton	1	1	1		1	
Marloffstein (Ms)	This study	Claystone pit	0.5	Amaltheenton	1	1	1			1
Mistelgau (Mg)	This study	Claystone pit and core	0.5	Jurensismergel	2	4	7		3	7
Reichenschwand (Rs)	This study	Claystone pit	0.5	Amaltheenton	1	1	1			1
Northern study area*	This study	Seismic survey	15.0–45.0	Liassic to Dogger				40		
Schönlind (Sl)	This study	Claystone pit	0.0	Amaltheenton	2	2	2		1	
Sengenthal (St)	This study	Claystone pit	0.5	Sengenthal Fm.	1	2	2			1
Unterstürmig (Us)	This study	Claystone pit	0	Amaltheenton		2	2		1	
Velburg (Vb)	ABDNB	Core	41.1	Eisensandstein to Sengenthal Fm.	3	7	14			
Zankschlag (Zs)	ABDNB	Core	57.1	Sengenthal Fm.	27	8	27			1
Zapfendorf (Zd)	Welz (1994)	Sonic log	20.5	Amaltheenton- to Jurensismergel Fm.				22		

Refraction velocities for low-velocity layers from a refraction seismic survey (see Fig. 1): Messenfeld – Unnersdorf (north of Bad Staffelstein); Hohengüßbach – Wildenberg (east of Braunach to south of Kronach); Draisdorf – Gottsfeld (west of Bad Staffelstein to west of Creußen). Abbreviations are as follows. ABDNB: Autobahndirektion Nordbayern; GSC: grain size classification; ρ_t: true (skeletal) density; ρ_b: bulk density; $\emptyset_{Hg}$: porosity derived from mercury intrusion porosimetry; v_P: P-wave velocity (in situ); VR: vitrinite reflectance; XRD: X-ray diffraction.

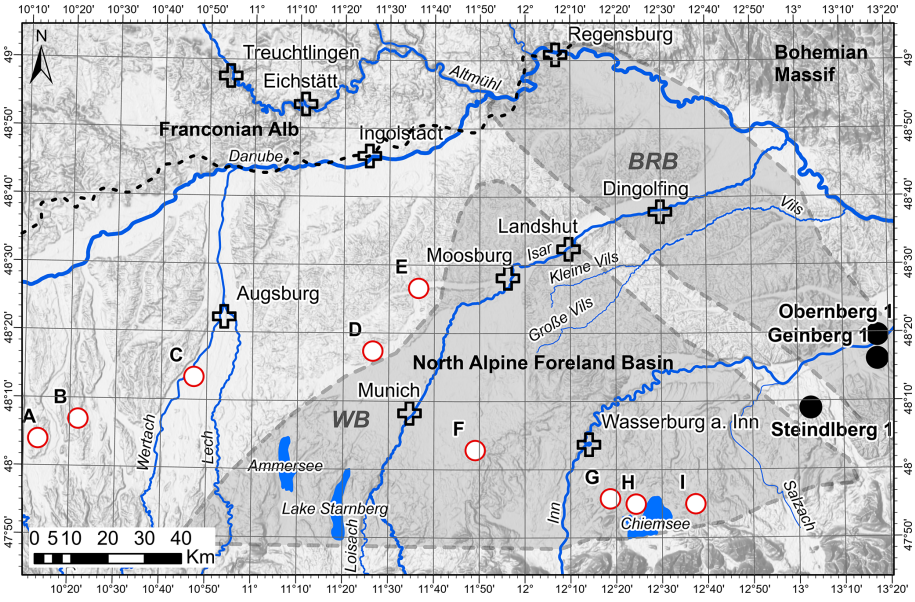

Figure 3. Map of the North Alpine Foreland Basin just south of our study area (see Fig. 1) including the Braunau–Regensburg Basin (BRB) and the Wasserburg Basin (WB) during the Late Cretaceous (adapted from Valečka and Skoček, 1991). The bold black dashed line in the Danube River area indicates the present-day erosional edge of the North Alpine Foreland Basin fill based on Bachmann and Müller (1992). White dots with red rims represent (anonymized) well locations (A to I) for which density and sonic log data are used in this study; black dots indicate well locations which were sampled for vitrinite reflectance (VR) measurements; white crosses mark larger cities. Modern drainage systems and lake bodies are highlighted in blue. Background lake and river data were provided by the European Environment Agency (EEA; status: published 23 February 2009, last modified 29 November 2012; downloaded 19 July 2021 at 12:36) and the Bundesanstalt für Gewässerkunde (WasserBLIcK/BfG and Zuständige Behörden der Länder, 1 April 2021; status: last updated 1 April 2021; downloaded 19 July 2021 at 14:08). Background data source: Earth Resources Observation And Science Center (2017).

al., 2006; Dewhurst et al., 1998; Vasseur et al., 1995) and is mainly controlled by grain size (Fawad et al., 2010; Mondol et al., 2007; Yang and Aplin, 2004), mineralogical composition (Fawad et al., 2010; Marion et al., 1992; Mondol et al., 2007), and texture (Fawad et al., 2010; Marion et al., 1992; Mondol et al., 2007). Strongly increased rock strength and velocity were observed for mudstones with high sand content and $< 40\,\%$ clay (Marion et al., 1992) as well as with elevated cement content (Horpibulsuk et al., 2010). These issues were considered in this study by measuring the mudstones' mineralogical composition and grain size distribution. As the mudstones' compaction behavior is thought to be almost irreversible even after unloading, they are particularly well suited to record maximum burial as well as overburden (e.g., Corcoran and Doré, 2005, Hillis, 1995; Menpes and Hillis, 1995) and have therefore frequently been applied in various studies (e.g., Baig et al., 2019; Henk, 1992; Issler, 1992). The degree of mudstone compaction is thereby best reflected in the rocks' (bulk and true) density, porosity, and ability to conduct acoustic pulse signals. All three parameters were determined or used in this study. Another source of information for maximum burial of mudstones is given by vitrinite reflectance, a measure of the increasing thermal maturation of organic matter contained in mudstones (Hertle and Littke, 2000; Liu et al., 2020; Sweeney and Burnham, 1990).

3.1 Mineralogy

For XRD-based whole rock mineralogical classifications, the dried mudstone samples were crushed and ground with the McCrone XRD mill and analyzed by an X-ray diffractometer D5000 (Siemens). A qualitative Rietveld analysis of the resulting signal was then done with the DIFFRAC.SUITE software EVA and thereafter semi-quantitatively with the DIFFRAC.SUITE software TOPAS 4.2 (both by Bruker).

3.2 Grain size analysis

Full disaggregation of the solid samples was achieved by applying the "saturation–freeze–thaw" method of Yang and Aplin (1997). Particle size analysis by sedimentation was done by applying a SediGraph III Plus by Micromeritics. The grain size classes are differentiated according to the geotechnical grain size classification scheme for soils (Deutsches Institut für Normung, 1987), whereby the clay fraction comprises particles $< 2\,\mu m$, the silt fraction particles of 2–63 µm, and sand particles are $> 63\,\mu m$. The grain size classification scheme follows Potter et al. (1980).

3.2.1 Mechanical compaction deduced from porosity–velocity relationships

Due to the mudstones' largely irreversible elastoplastic compaction behavior, the degree of mechanical mudstone compaction provides a good first-order estimate of the maximum mean effective stress (e.g., Corcoran and Doré, 2005; Goulty, 1998; Hillis, 1995) and hence the maximum burial depth, thereby assuming that the vertical stress represents the largest principal stress and the vertical effective stress gradient is known.

Mechanical compaction in terms of porosity decrease and velocity increase in both Mesozoic and Cenozoic mudstones from the North Alpine Foreland Basin has been previously investigated as a function of vertical effective stress by Drews et al. (2018). The North Alpine Foreland Basin is situated directly south of the study area (Figs. 1 and 3), and uplift since maximum basin subsidence is estimated not to have exceeded more than ~ 500 m there (Baran et al., 2014; Drews et al., 2018; Kuhlemann and Kempf, 2002; Zweigel et al., 1998). Thus, the depth-related increase in mudstone compaction in the North Alpine Foreland Basin (NAFB) is likely a good analogue for our study area. Drews et al. (2018) determined a mudstone compaction trend, which utilizes porosity decay as a function of vertical effective stress, based on the exponential compaction law of Athy (1930) (Eq. 1):

$$\text{Ø}_{\text{sh}} = \text{Ø}_{0\_\text{sh}} \times \text{Exp}\,(-\text{VES}/C)\,. \quad (1)$$

Equation (1) is the porosity decay function of Athy (1930) modified for vertical effective stress (VES) according to Heppard et al. (1998), Rubey and Hubbert (1959), and Scott and Thomsen (1993). Ø_{sh} is the mudstone porosity at a particular depth. Following Drews et al. (2018) the mudstone porosity at the surface Ø_{0_sh} was set to 0.4 (dimensionless) and the compaction coefficient C to 31 MPa^{-1}.

The porosity–velocity relationship proposed by Raiga-Clemenceau et al. (1986) can then be used to derive a velocity vs. vertical effective stress relationship:

$$v_{\text{P}} = v_{\text{P}_{\text{shm}}} \times (1 - \text{Ø}_{\text{sh}})^{x}. \quad (2)$$

Equation (2) is the mudstone porosity–velocity relationship of Raiga-Clemenceau et al. (1986), wherein v_{P} is the P-wave velocity in mudstones. For the NAFB, Drews et al. (2018) set the matrix velocity of mudstones $v_{\text{P}_{\text{shm}}}$ to 5076 m s^{-1} and x to 2. Alternatively, Ø can be substituted by the water-saturated mudstone bulk density $\rho_{\text{b\_sat}}$ using the following relationship:

$$\rho_{\text{b\_sat}} = \rho_{\text{t}} \times (1 - \text{Ø}) + \rho_{\text{f}} \times \text{Ø}, \quad (3)$$

where ρ_{t} is the true or skeletal density of the mudstone and ρ_{f} is the density of the pore-filling fluid with 1.0 g cm^3 for water. The maximum burial depth TVD_{max} can then be estimated from VES:

$$\text{TVD}_{\text{max}} = \text{VES}/\text{VES}_{\text{grad}}, \quad (4)$$

with the vertical effective stress gradient VES_{grad} typically varying between 10 and 16 MPa km^{-1} in hydrostatically pressured sedimentary basins, derived from a vertical stress gradient of 20–26 MPa km^{-1} and a hydrostatic pore pressure of 10 MPa km^{-1} (Bjørlykke, 2015). For the NAFB, Drews et al. (2018, 2020) determined a vertical effective stress gradient of 13 MPa km^{-1}, which will also be used for depth calculations in this study.

3.2.2 Porosity and density

Dry bulk densities $\rho_{\text{b\_dry}}$ and porosities Ø_{Hg} of 72 claystone and mudstone samples have been measured with a mercury intrusion porosimeter (Poremaster 60 by Quantachrome), which analyzes pore diameters in the range of 0.0036–950 µm under pressures of up to 60 000 psia. Prior to measurements, samples were dried at 65 °C until no change in mass could be determined for 24 h. Thereby, cracks may have formed during sample preparation and dehydration (Klaver et al., 2012). In turn, this might result in the intrusion of mercury into these cracks at low pressures, but associated data excursions are rather obvious and were removed prior to further analysis as proposed by Klaver et al. (2015). True (skeletal) densities ρ_{t} were determined for a subset of 41 samples by applying helium pycnometry (Accupyk II 1345 by Micromeritics), which enables analysis of pores even smaller (0.22 nm) than mercury (3.6 nm) (Hedenblad, 1997; Krus et al., 1997). For samples lacking direct ρ_{t} measurements, the mean true density $\rho_{\text{t\_mean}}$ was used for further calculations. Using bulk density $\rho_{\text{b\_dry}}$ and true density ρ_{t} as well as $\rho_{\text{t\_mean}}$ the (effective) porosity Ø_{calc} was calculated:

$$\text{Ø}_{\text{calc}} = 1 - \frac{\rho_{\text{b\_dry}}}{\rho_{\text{t\_mean}}}. \quad (5)$$

3.2.3 Velocity modeling based on density and porosity measurements

Applying the porosity–velocity relationship (see Eq. 2) proposed by Raiga-Clemenceau et al. (1986) and the velocity–density relationship by using density instead of porosity values (see Eq. 5) then allows for the calculation of mudstone velocities. Calculating mudstone velocities from Ø_{calc} yields $v_{\text{P}_{\text{calc}}}$, while mudstone velocities based on measured Ø_{Hg} values are labeled $v_{\text{P}_{\text{calc-Hg}}}$.

3.2.4 Mudstone velocity

In situ mudstone velocities v_{P} were derived from near-surface (15–45 m TVD, see Table 1) seismic refraction data acquired in the course of this study (see locations in Fig. 1), published borehole geophone measurements (Buness and Bram, 2001), and downhole sonic log readings (Welz, 1994).

3.3 Vitrinite reflectance

Random vitrinite reflectance in oil (VR) was determined for 11 selected samples (Table 1) using a magnification of 100× in non-polarized light at a wavelength of 546 nm (Taylor et al., 1998). Yttrium–aluminum–garnet ($R = 0.899\,\%$) and gadolinium–gallium–garnet ($R = 1.699\,\%$) standards were used for calibration. As the vitrinite maturation is mainly affected by temperature as well as by the duration of maximum burial (Nöth et al., 2001) and only to a minor degree by pressure (Hunt, 1979), these measurements are strongly dependent on the evolving heat flow and therefore the geothermal gradient within a sedimentary basin (Suggate, 1998). Vitrinite reflectance depth profiles therefore have to be set up for a specific region of interest. However, heat flow and resulting geothermal gradient may have changed over time, and there are variables like the respective organofacies or the individual reaction kinetics which may influence the transformation and ordering processes of vitrinites (Le Bayon et al., 2011). A VR depth trend was constructed based on published vitrinite reflectance data (Gusterhuber et al., 2012) and partly unpublished data for Cretaceous mudstones in the northern part of the NAFB in Austria, where the samples' burial depths were known to allow calibration (Fig. 3). From the correlation between the measured sample vitrinite reflectance and the VR depth trend, the burial depth of Franconian Alb claystones and mudstones was inferred. As the Mesozoic burial history of the northern part of the Upper Austrian Molasse Basin (Nachtmann and Wagner, 1987) is rather similar to the Franconian Alb area (Peterek et al., 1997; Schröder, 1987), a comparison between our samples and the developed VR depth trend is considered to be reasonable.

4 Results and discussion

4.1 Mudstone composition

A total of 41 claystone and mudstone samples were analyzed in terms of their grain size classification (Fig. 4a) and 37 regarding their mineralogical composition (Fig. 4b) to ensure that we base our study on a rather homogeneous sample set in terms of grain size and mineralogical composition.

4.1.1 Grain size classification

Most of the claystone pit samples contain $< 10\,\%$ of grains $> 63\,\mu m$ (sand fraction), 40 %–60 % of grains in the range 2–63 µm (silt fraction), and 40 %–60 % of grains $< 2\,\mu m$ (clay fraction). Therefore, the majority of samples are classified as "mudstones" or "claystones" (Fig. 4a). Exceptionally high clay fraction percentages were observed for few samples from the claystone pit Großheirath as well as for core samples from Mistelgau and Zankschlag (Fig. 4a). The fact that cores from one well location were sampled at various depth levels explains the large spread in grain size classifications, particularly for the Zankschlag well samples, for which several meters of cores were analyzed. Two Zankschlag core samples with increased sand and decreased clay contents (Fig. 4a) were excluded from further analysis as they are classified as sandy mud shales rather than "pure" mud or clay shales in the classification scheme of Potter et al. (1980). This is because major deviations in petrophysical properties (e.g., porosity and P-wave velocity) of mudstones and compaction behavior are reported for samples with increasing sand admixture and $< 40\,\%$ clay content (Marion et al., 1992).

4.1.2 Mineralogical composition

Clay mineralogical studies of marine Jurassic clays and marls in our study area by Krumm (1965) have shown a dominance of illite and muscovite over kaolinite and low quantities of chlorite and vermiculite. Mineral compositions hardly vary even over large distances, and compositional variations are only observed among different stratigraphic units. Clay-mineralogy-based mudstone compaction should therefore be relatively uniform for the investigated mudstone samples and hence comparable to each other. The mineralogical compositions of analyzed claystone and mudstone samples are shown in Fig. 4b. There is a very limited range of variation between the individual claystone pit samples, most of which contain on average 44 wt % clay minerals besides ~ 42 wt % accessory minerals (mainly quartz, pyrite, or rutile) and 14 wt % carbonate minerals. In most samples, the amount of carbonate minerals was low and in the range of 2 wt %–14 wt %. Samples that contained > 40 wt % of calcareous minerals were excluded from further analysis. Increased calcite content in mudstones is often associated with early cement stabilization, leading to increased strength (Horpibulsuk et al., 2010) that might counteract mudstone compaction during burial.

4.2 Mudstone velocity data

Compressional P-wave velocities of Jurassic mudstones, which have been retrieved from shallow seismic refraction surveys (see locations in Fig. 1) and sonic log data for the shallow Zapfendorf borehole (Welz, 1994) (Table 1), increase and converge towards velocities of 2000–3500 $m\,s^{-1}$ at depths of 15 m below ground level (Fig. 5a). We infer from this that below a depth of 15 m, unloading-related processes are negligible and therefore selected only velocities from depth > 15 m for further analysis.

Mudstone velocity vs. true vertical depth (TVD) plots for normally pressured Mesozoic and Cenozoic mudstones in the NAFB (Drews et al., 2018; their Fig. 4) show that mudstone compaction can be approximated by a single trend with the calculated normal compaction trend (NCT) derived from the combination of a modified Athy equation (see Eq. 1) and the porosity–velocity transform (see Eq. 2) of Raiga-Clemenceau et al. (1986). Drews et al. (2018) also deter-

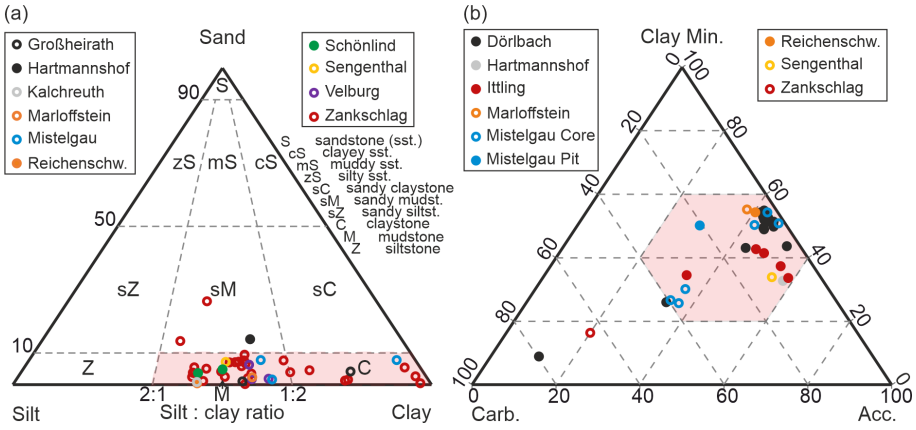

Figure 4. (a) Grain size classification of mudstone samples (according to Potter et al., 1980; plot layout modified from Lindholm, 2012) with sand (> 63 µm), silt (2–63 µm), and clay (< 2 µm) fractions as endmembers of the ternary plot. Only samples within the fields colored in red were used for further measurements. **(b)** Ternary plot of XRD-based mudstone composition illustrating relative abundance of clay minerals (e.g., illite, smectite, kaolinite, chlorite), carbonate minerals (e.g., calcite, dolomite, ankerite, siderite), and accessory minerals (Acc.) including quartz, pyrite, and rutile. Only samples within the reddish boxes were included in further analysis.

mined the systematic depth-dependent velocity increase in Mesozoic and Cenozoic mudstones as a function of vertical effective stress (derived from in situ measured pressures from drill stem, production, and wire-line formation tests as well as associated mudstone velocities), well captured by the calculated NCT on a basin-wide scale (Fig. 5b).

Relating maximum mudstone velocities of 2500–3500 m s^{-1}, measured in Jurassic mudstones of the Franconian Alb area (Fig. 5a), to the NCT established by Drews et al. (2018; their Fig. 4) suggests vertical effective stresses in the range of 10–25 MPa (Fig. 5b) and roughly equates to 700–2000 m true vertical depth.

4.3 Integrating mudstone porosity and velocity data

Dry bulk densities ρ_{b_dry} and porosities $Ø_{Hg}$ were analyzed from 72 samples by Hg intrusion porosimetry, and true (skeletal) densities ρ_t with an average value ρ_{t_mean} of 2.73 ± 0.06 g cm^{-3} (Fig. 6a) for 34 clay pit and shallow drill core samples (Table 1) were determined by He pycnometry. Mudstone porosities were also calculated ($Ø_{calc}$) based on bulk densities ρ_{b_dry} and true (skeletal) densities ρ_{t_mean} (Eq. 5).

We preferred the calculated porosity values rather than Hg porosities because continued mercury intrusion even at the device's maximum injection pressure (see inset in Fig. 6b) suggested that micropores < 0.003 µm were not fully involved in the measurement. The cross-plot of calculated porosities $Ø_{calc}$ versus measured porosities $Ø_{Hg}$ reveals major discrepancies due to the incomplete involvement of micropores by using Hg porosities (Fig. 6b). The relation between downhole mudstone velocities and bulk densities is well captured by the NCT established by Drews et al. (2018) (Fig. 7a). Figure 7b compares mudstone velocities $v_{P_{calc}}$ with $v_{P_{calc\text{-}Hg}}$. The values reveal a positive linear relationship, but with significant diversions towards faster $v_{P_{calc\text{-}Hg}}$ values and a clustering of $v_{P_{calc}}$ values at 3000–3500 m s^{-1} (Fig. 7b).

As shown by the box plot summary (Fig. 8a), calculated mudstone velocities $v_{P_{calc}}$ applying $Ø_{calc}$ are considerably lower (average 3300 m s^{-1}) than $v_{P_{calc\text{-}Hg}}$ applying $Ø_{Hg}$ (average 3900 m s^{-1}) due to the incomplete involvement of micropores in $Ø_{Hg}$-based calculations (see Figs. 6b and 7b). Calculated mudstone velocities $v_{P_{calc}}$ are higher compared to in situ measured mudstone velocities derived from seismic refraction surveys ($v_{P_{seis}}$ average 2600 m s^{-1}) and shallow sonic log data ($v_{P_{log}}$ average 2800 m s^{-1}) from the Franconian Alb area. This is most likely method-related, as $v_{P_{calc}}$ values represent lab-based measurements on small, homogeneous sample volumes which are analyzed under controlled conditions, while in situ measured velocities refer to larger volumes and are hence probably influenced by factors such as variations in (de-)compaction, pore water saturation, weathering, and discontinuities. Hence, the main discrepancy between the applied methods results from the methods' differing sensitivity to these factors, with the in situ measured velocities being highly susceptible in contrast to the lab-based measurements.

Referencing mudstone velocities to the mudstone velocity trend of Drews et al. (2018) derived from hydrostatically pressured mudstones in the NAFB (Fig. 5b) views v_P values as a function of vertical effective stress (VES). Any uplift, although reported < 500 m for the mudstones in the North Alpine Foreland Basin (Baran et al., 2014), could lead to an underestimation of our burial depth estimation by the respective amount but will be neglected in our calculations as it is within the range of uncertainty. The majority of field velocity data from seismic refraction survey $v_{P_{seis}}$ and shallow sonic log data $v_{P_{log}}$ (Welz, 1994) indicate a paleo-vertical effective stress in the range of 7–19 MPa (average 10 MPa for

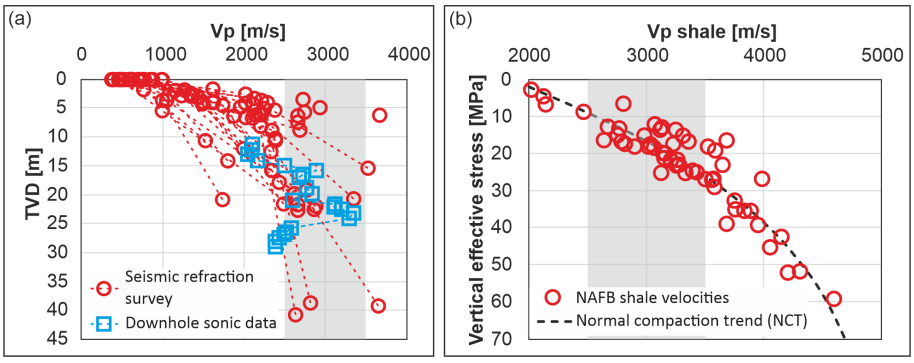

Figure 5. (a) Claystone and mudstone velocities from field measurements in the Franconian Alb area versus true vertical depth (TVD); data sources are shallow seismic refraction surveys (this study) and downhole sonic log data for the shallow Zapfendorf well (Welz, 1994). **(b)** Mudstone velocities from sonic log and vertical seismic profile (VSP) data for deep wells in the North Alpine Foreland Basin (NAFB) as a function of vertical effective stress (derived from drill stem and production tests as well as wire-line formation pressure tests) (redrawn from Drews et al., 2018). All data shown represent hydrostatically pressured mudstone sections. The black dashed line represents the normal compaction trend (NCT) determined by Drews et al. (2018). The grey background boxes mark the maximum velocity range of claystones and mudstones determined by field measurements in the Franconian Alb area.

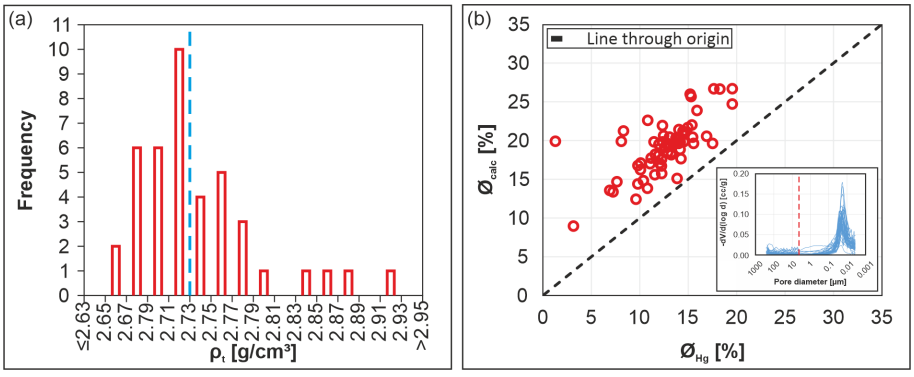

Figure 6. (a) Histogram of true densities ρ_t of mudstones of the Franconian Alb derived from helium (He) pycnometry, yielding an average value of 2.73 g cm^{-3} (vertical red dashed line). **(b)** Porosities derived from Hg intrusion porosimetry $Ø_{Hg}$ versus calculated porosities $Ø_{calc}$ based on the quotient of bulk densities ρ_{b_dry} and mean true densities ρ_{t_mean}. The inset indicates continued mercury intrusion even at the device's maximum injection pressure, suggesting that Hg intrusion porosimetry does not include the entire micropore spectrum. Porosity that was potentially induced by drying or unloading effects (to the left of the red dashed line) was removed from the porosity $Ø_{Hg}$ calculation.

seismic refraction and 14 MPa for sonic log), while calculated velocities $v_{P_{calc}}$ and $v_{P_{calc\text{-}Hg}}$ yield higher values in the range of 13–46 MPa (average 23 MPa) and 22–90 MPa (average 36 MPa), respectively (Fig. 8b). This could be due to the scale of the measurement: while the in situ field velocity data were measured roughly on a meter scale and most likely also captured larger unloading structures due to the shallow present-day burial depth, the measured porosity data are derived from centimeter-sized samples, which most likely are not as affected by unloading, and if such effects were recognized they were removed from the analysis (see caption of Fig. 6).

Applying an average vertical effective stress gradient of 13 MPa km^{-1} to field velocity data of mudstones $v_{P_{seis}}$ and $v_{P_{log}}$ yields a maximum burial depth for Franconian Alb area samples of 0.0–1.8 km (0.9 ± 0.4 km mean), whereas $v_{P_{calc}}$ and $v_{P_{calc\text{-}Hg}}$ yield 1.0–3.6 km (1.8 ± 0.4 km mean) versus 1.7–6.9 km (2.8 ± 0.8 km mean) burial, respectively (Table A1). A lower stress gradient, associated with a less consolidated overlying rock column, would result in elevated maximum burial depths. In the unlikely case of a higher stress gradient, reflecting an overlying rock column of much denser lithology, this would yield decreased maximum burial depth values. Therefore, the applied VES gradient of 13 MPa km^{-1} and resulting maximum burial depth values represent a lower bound. Hence, depth-corrected field velocity data and lab porosity data based on $Ø_{Hg}$ suggest that about 0.2–0.8 km (0.3 km mean) and 1.8–2.4 km (2.2 km mean) of post-Jurassic sediments were removed in the Franconian Alb area since deposition (Fig. 8c). Lab porosity data $Ø_{calc}$, however, are considered more reliable and suggest 1.0–1.4 km (1.1 km mean) of post-Jurassic overburden.

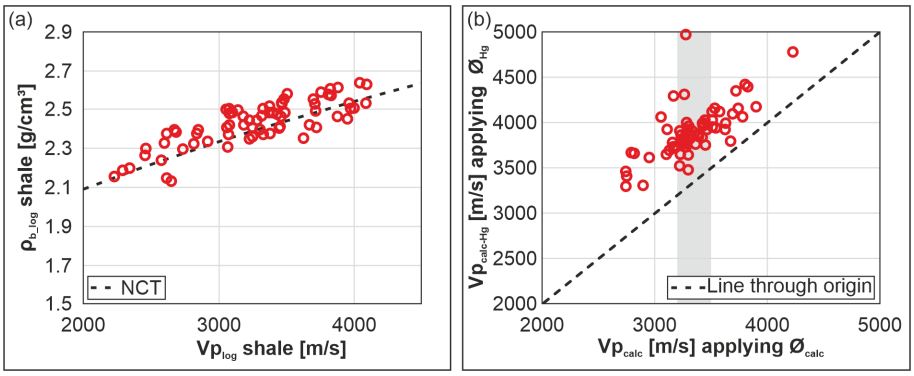

Figure 7. Mudstone velocity–density model. **(a)** P-wave velocity ($v_{P_{log}}$) from sonic log and vertical seismic profile data as a function of bulk density log data ρ_{b_log} of deep wells in the NAFB (after Drews et al., 2018). The black dashed line represents the NCT of Drews et al. (2018). **(b)** Calculated mudstone velocities $v_{P_{calc}}$ applying $Ø_{calc}$ vs. $v_{P_{calc\text{-}Hg}}$ using $Ø_{Hg}$. The grey bar highlights clustering of $v_{P_{calc}}$ values at 3000–3500 m s^{-1}.

All these values must be corrected by their actual sample burial depth. However, instead of subtracting individual corrections for the Upper Jurassic strata thickness at each sample location, an average value was removed. This is related to the fact that only remnants of Upper Jurassic limestones are preserved with up to 200 m thickness, but an unknown amount of Upper Jurassic sediments was eroded in large parts of the Franconian Alb. Hence, their original paleothicknesses can only be inferred from seismic data in the NAFB, where Bachmann et al. (1987) determined a general value of 0.6 km for the thickness of the Upper Jurassic Malm unit. This thickness was thus removed from the calculated burial depth values.

Furthermore, no samples were corrected for their distances to the Middle Jurassic–Upper Jurassic interface at each location. As the Upper Jurassic limestones are missing at most sample locations, so is the knowledge of the actual distance to the Middle Jurassic–Upper Jurassic interface. Estimates for the former position of this interface in the Franconian Alb area were only done by von Freyberg (1969). As the majority of the investigated samples are of Middle Jurassic age, only interpolated values based on a georeferenced map from von Freyberg (1969) are available for the sample locations. Because of the thicknesses of Middle Jurassic sediments of 20–170 m or even less (Meyer and Schmidt-Kaler, 1996), we consider the neglect of these sediments to lie within the uncertainty range and did not include them in the calculation of the removed sediment columns in Fig. 8c. A summary of burial depth and amount of removed sediment calculated at each sample location, based on a variety of different input parameters, is given in Table A1.

4.4 Vitrinite reflectance

Vitrinite reflectance values of Upper Triassic to Middle Jurassic mudstone samples from the Franconian Alb vary between 0.32 % Ro and 0.61 % Ro with a mean of 0.49 % Ro and a correlation coefficient of $R^2 = 0.76$ with true vertical depth (TVD) (Fig. 9). As no information on the paleoheat flow in this region is available, no vitrinite reflectance evolution with depth could be modeled for the study area. However, a comparable VR depth trend is derived from published (Sachsenhofer, 2001) and unpublished (R. F. Sachsenhofer, written communication, 2021) vitrinite reflectance data for Upper Triassic to Middle Jurassic mudstones from the northern part of the NAFB in Austria (Fig. 3). Our results can be related to these, as they presumably have a similar thermal history. Samples from the Austrian part of the NAFB show vitrinite reflectances of 0.3 % Ro–0.6 % Ro developed at sampling depths of ∼ 800–2200 m (Fig. 9). Applying this VR depth trend to Franconian Alb VR data reveals a similar paleo-burial depth range of 800–2200 m for the Franconian Alb area samples. Hence, applying VR data, our Lower Jurassic Franconian Alb samples probably experienced a maximum burial depth average of ∼ 1650 m, and, considering ∼ 600 m thickness for Upper Jurassic sediments, a removed post-Jurassic sediment column of ∼ 1050 m is calculated.

4.5 The Franconian Alb burial history in a regional context

Our burial depth calculations for the Early to Middle Jurassic mudstones of the Franconian Alb area suggest a burial depth of at least 900 m, based on downhole and shallow seismic refraction mudstone velocities, but rather ∼ 1700 m as inferred from calculated porosities $Ø_{calc}$ and VR data as any unloading and drying effects can be ruled out in these datasets (Fig. 10). A strong overestimation of maximum burial depths derived from $Ø_{Hg}$ porosity values is displayed in Fig. 10c but has low reliability due to the incomplete micropore involvement (Fig. 6b). As the thicknesses of Early Jurassic strata (∼ 20 m in the southern and ∼ 100 m in the northern Franconian Alb), Middle Jurassic strata (∼ 150 m:

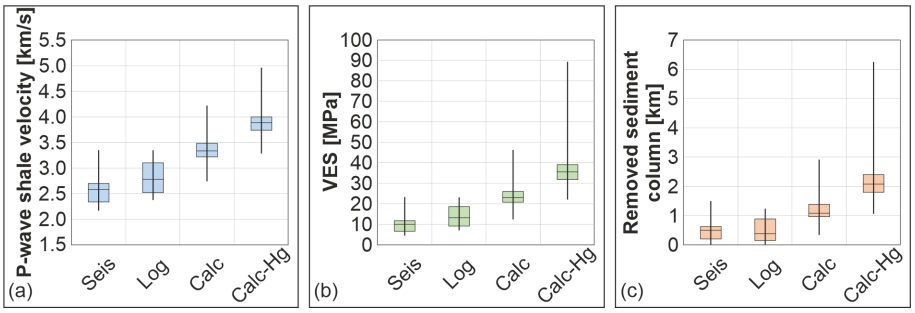

Figure 8. Box plot summary of mudstone compaction results in the Franconian Alb area. **(a)** Box plot summary of measured and calculated mudstone velocity ranges from shallow seismic refraction data $v_{P_{seis}}$ (Seis), shallow sonic log data $v_{P_{log}}$ (Log) (Welz, 1994), and calculated velocity $v_{P_{calc}}$ applying $Ø_{calc}$ (Calc) and $v_{P_{calc\text{-}Hg}}$ applying measured $Ø_{Hg}$ values (Calc-Hg). **(b)** Same as **(a)**, but velocities have been referenced to equivalent vertical effective stress (VES) according to the normal mudstone compaction trend (NCT) of Drews et al. (2018) in the NAFB. **(c)** Same as **(b)**, but showing thickness ranges of removed post-Jurassic sediment columns when applying an average vertical effective stress (VES) of 13 MPa km^{-1}. An average thickness of 0.6 km has been subtracted for removed Upper Jurassic (Malm) sediments.

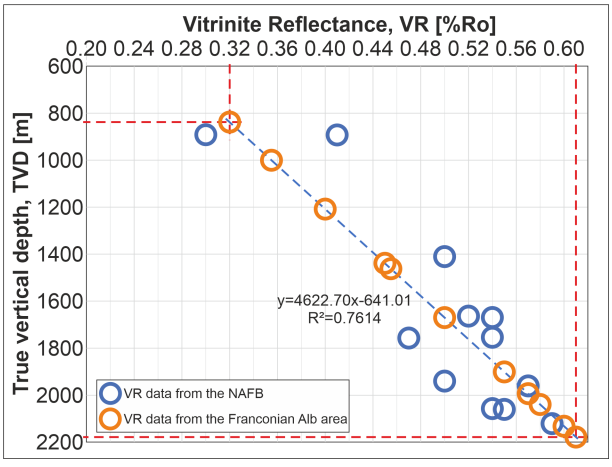

Figure 9. Comparison of Franconian Alb area VR data (this study) to the VR depth trend (TVD) derived from published (Sachsenhofer, 2001) and unpublished vitrinite reflectance data (R. F. Sachsenhofer, written communication, 2021) of the northern, Austrian part of the NAFB. R^2 is the coefficient of determination. The range of vitrinite reflectance values of our samples and inferred burial depths of ca. 800–2200 m is indicated by the red dashed lines.

Meyer and Schmidt-Kaler, 1996), and Late Jurassic sediments (∼ 600 m in the neighboring NAFB: Bachmann et al., 1987) are roughly known, cumulative Jurassic sediment thicknesses are subtracted from maximum burial depth to get values for removed post-Jurassic (Cretaceous plus Cenozoic) sediment thicknesses. The maximum overburden results for each location in the Franconian Alb area and each calculation method are listed in Table A1.

Our vitrinite reflectance data (Fig. 10a and d), indicating burial depths of 0.8–2.2 km (mean 1.7 km), correlate very well with burial depth of ∼ 1.7 km inferred from calculated porosities $Ø_{calc}$ applying He-pycnometry-derived mean true densities ρ_{t_mean} and bulk densities ρ_b (Fig. 10b) (see Table A1).

West of the Franconian Line, AFT data (Hejl et al., 1997) as well as field-mapping- and literature-based interpretations (sedimentological studies, thermochronological data, radiometric age data, etc.) suggest deposition and subsequent removal of > 1000 m of Cretaceous and Cenozoic sediments (Peterek and Schröder, 2010; Schröder, 1987; Schröder et al., 1997), of which only ca. 320 m of Upper Cretaceous strata is preserved (Dill, 1995). Hence, compared to the more distal western parts of the Franconian Alb, strongly increased depositional thicknesses along the front of the Franconian Line can be considered due to the uplift and major exhumation of the Bohemian Massif to the east, combined with westward thrusting and syntectonic deposition of the eroded material (Meyer, 1996; Peterek and Schröder, 2010).

Results of the AFT and (U−Th)/He analysis of von Eynatten et al. (2021), on the other hand, suggest burial depths of 3.0–4.0 km for exposed Triassic sedimentary rocks in large parts of central Germany, including the Franconian Alb. Applying these values, about 0.9 km of Jurassic and 2.1–3.1 km of Cretaceous–Cenozoic sediments would have been removed, which exceeds our estimations for removed Cretaceous–Cenozoic sediments (deduced from both the calculated porosities $Ø_{calc}$ and the VR data) by ∼ 1.1 km. This discrepancy can be explained either by the fact that von Eynatten's Franconian Platform sample locations, ca. 20 km to the north of our study area, experienced a different subsidence and/or burial history or by the applied geothermal gradient which von Eynatten et al. (2021) estimated at only 30 °C km^{-1}. This gradient contrasts with an elevated regional geothermal gradient of 38 °C km^{-1} determined by de Wall et al. (2019) in the vicinity of the Franconian Alb close to Mistelgau. Elevated geothermal gradients of > 40 °C km^{-1} are also observed in the area around Mürsbach (Bauer, 2000; Kämmlein et al., 2020). If the increased geothermal gradient also applies to the area investigated by

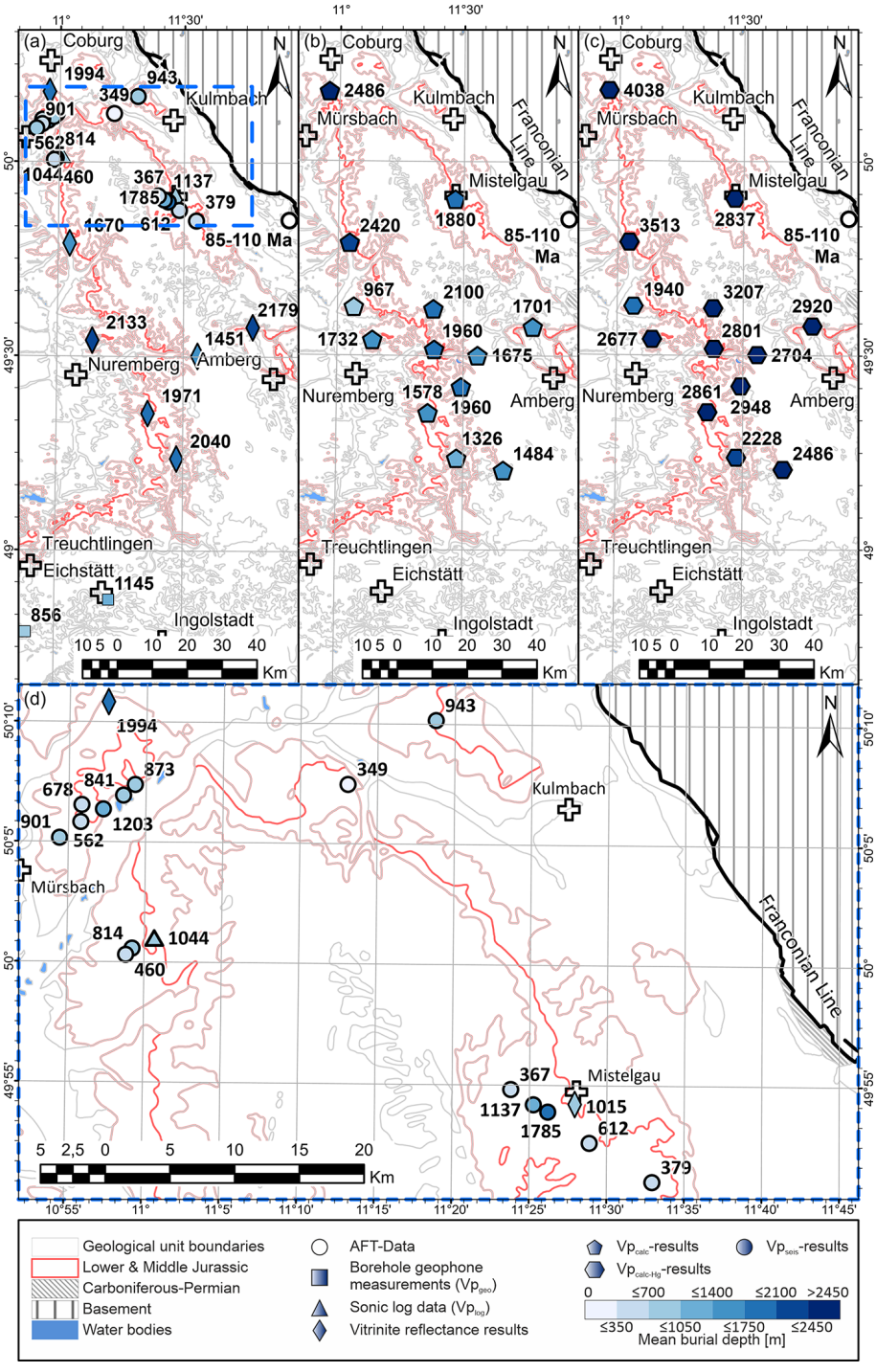

Figure 10. Areal distribution of calculated mean burial depth of sampled Lower–Middle Jurassic mudstones in the Franconian Alb area based on two different methods: **(a)** burial depths derived from the correlation between the NCT of Drews et al. (2018) and reliable in situ P-wave velocities, including shallow seismic refraction data ($v_{P_{seis}}$), shallow sonic log data ($v_{P_{log}}$: Welz, 1994), and borehole geophone data ($v_{P_{geo}}$; Buness and Bram, 2001). Furthermore, burial depth calculations based on the correlation between the NAFB derived VR depth trend and Franconian Alb area VR data are included. **(b)** Burial depths inferred from $v_{P_{calc}}$ based on porosities $Ø_{calc}$. **(c)** Burial depths inferred from $v_{P_{calc\text{-}Hg}}$ based on porosities $Ø_{Hg}$. **(d)** Detailed map of the blue dashed box in **(a)**. Fills of sampling points according to color scheme for total eroded thicknesses. See Table A1 for detailed results. Background data source: Bayerisches Landesamt für Umwelt, https://www.lfu.bayern.de/index.htm (last access: 17 January 2017).

von Eynatten et al. (2021), significantly lower burial depths would result in their calculations. However, the elevated geothermal anomaly is rather focused in an area ca. 20 km north of Bamberg (Fig. 1) and quickly diminishes towards the south and east, where the gradient varies between 25 and 31–37 °C km^{-1} according to Bauer (2000) and a typical regional heat flow of 65–85 mW m^{-2} prevails (Čermák and Bodri, 1991). Von Eynatten et al. (2021) also state that the magnitudes of exhumation and erosion are remarkably reduced towards the eastern Franconian Alb margin. We therefore think that our estimates of removed post-Jurassic sediments for the Franconian Alb area are more realistic and do not contradict but rather support and complement the results of von Eynatten et al. (2021). Bachmann et al. (2002) argue that no Cretaceous sediments were deposited in the western part of the Franconian Alb area. This conclusion can most likely be related to the more distal-to-source position of their study area, positioned between Tübingen and Würzburg, compared to ours (Franconian Alb area). As Cretaceous sediments in the Franconian Alb area were most likely sourced from the Bohemian Massif towards the east (Niebuhr et al., 2011, 2012; Schröder, 1987; Schröder et al., 1997; Voigt et al., 2008), a reduced sediment supply to positions more distal to the source can be expected. Westward decreasing Cretaceous sediment columns, as proposed by Meyer (1996) and Peterek and Schröder (2010), support this interpretation.

4.6 Spatial distribution of post-Jurassic sediment overburden

The lateral variation of calculated burial depths derived from two independent datasets (Fig. 10a–d) shows no regional trends or noticeable areas of increased or reduced burial depth. Only in the case of the porosity-derived burial depth estimations (Fig. 10b) can a trend towards increased amounts of post-Lower Jurassic paleo-thickness in the northwestern part of the Franconian Alb be conjectured, though this impression is based on sparse data density in the area of interest.

Additional information comes from published AFT and measured VR data. From the VR results, no distinct differential vertical movements between various parts of the Franconian Alb can be inferred. According to von Eynatten et al. (2021), however, AFT and (U−Th)/He data indicate that Triassic sediments were less deeply buried next to the Bohemian Massif boundary in the east ($\ll$ 3–4 km) compared to the central part of their study area (3–4 km), situated close to the Franconian Line. The discrepancy with our results ($\sim$ 1 km) can be explained by the doming model of von Eynatten et al. (2021), as their analyzed Franconian Platform sample set was taken closer to the doming center, which is located further to the north of our study area. Hence, our study area was most likely less affected by doming-related processes. The AFT results of Hejl et al. (1997) and the sedimentological observations of Schröder (1987) and Peterek and Schröder (2010) additionally suggest that higher sediment thicknesses ($\sim$ 2 km) were deposited directly west of the Franconian Line compared to the more distal-to-source parts. The more distal-to-source locations of the majority of our samples most likely explain these reduced burial depths. Reasons for reduced sediment removal in the southwestern part of the study area are given by Peterek and Schröder (2010). They suggest temporarily reduced erosion rates in this area due to the coverage by Neogene lake sediments that protected underlying Mesozoic sediments from erosion.

Information on the timing of sediment deposition and removal in the study area could not be inferred from our data, but this issue has been investigated by various authors (Peterek and Schröder, 2010; Schröder, 1987; Schröder et al., 1997; Ziegler, 1987). Early Cretaceous sediments (Late Valanginian to Barremian) constitute, if at all, only minor to negligible ratios of the original sediment column and were most likely already removed during the Late Valanginian to Cenomanian erosional event (Schröder, 1987). Sedimentation resumed during the Cenomanian–Turonian to Campanian (Ziegler, 1987; Meyer, 1981, 1989a, b), and related deposits must have constituted the majority of the eroded sediments, as sedimentation in most parts of the study area ceased thereafter (Peterek and Schröder, 2010). This termination in sedimentation was superseded by the profound erosion of Cretaceous sediments, caused by the latest Cretaceous to Paleocene inversion (Schröder, 1987; Schröder et al., 1997). Uplift associated with thermal doming of the Bohemian Massif probably continued after the Miocene, resulting in the absence of widespread sediment cover in the study area (Peterek and Schröder, 2010; Schröder, 1987; Schröder et al., 1997).

In summary, our data suggest that considerable amounts of post-Jurassic sediments must have been removed from the investigated area. Having information on the paleo-stress conditions during burial of now surface-exposed sedimentary rocks is key for relating their petrophysical properties to their deeply buried analogues. Our results indicate that the Upper Jurassic "Malm" carbonates, which are exposed in the Franconian Alb area and plunge southwards to depths of up to 5500 m in the Alpine foreland (Bachmann et al., 1987), constitute suitable analogues for reservoirs drilled at equivalent burial depths of $\sim$ 1050 m in the NAFB. This would directly apply to the geothermally productive Malm reservoirs in the proximal north of Munich and in the Moosburg–Landshut area (Fig. 3).

5 Conclusions

This study aimed to quantify eroded thicknesses of post-Jurassic sediments that were originally deposited in the Franconian Alb area, forming the southeastern part of the German Basin. We thereby took advantage of the presence of widely distributed Lower Jurassic mudstones and their inelastic

compaction behavior, recording maximum burial depth well by their petrophysical properties. From various locations distributed over the Franconian Alb, a large number of mudstone density and porosity measurements were performed and complemented by vitrinite reflectance and both new and published in situ P-wave velocity data from seismic surveys and downhole logging. These datasets were subsequently related to a compaction depth trend that was calibrated on mudstones of the same stratigraphic unit in the NAFB to the south of our study area. From the velocity data, we conclude that the Lower–Middle Jurassic mudstones experienced a maximum overburden of ~ 900 m, ~ 600 m of which relates to Upper Jurassic and only ~ 300 m to post-Jurassic sediments. More likely, however, are mean values of about 1100 m (total range 900–1400 m) of eroded Cretaceous–Cenozoic sediment thicknesses deduced from lab-based porosity and bulk density measurements as these rock parameters are less influenced by alteration, unloading effects, and variable water saturation of in situ measured samples. Hence, near-surface in situ P-wave velocity data need to be treated with caution – in our case they were not suitable for reliable burial depth estimations. Vitrinite reflectance data essentially confirm burial depths of ~ 1050 m post-Jurassic overburden ($\sim$ 1650 m for Lower–Middle Jurassic mudstones) derived from lab-based porosity and bulk density measurements. No clear trends for a lateral variance in reconstructed post-Jurassic sediment thicknesses were observed, although porosity- and bulk-density-derived maximum burial depths suggest a slight thickness increase towards the northwest.

The results of this study contribute to the post-Jurassic burial history of the Franconian Alb region. We also realized that maximum burial calculations, based solely on refraction velocity measurements of near-surface mudstone samples, may be heavily disturbed by relaxation and dehydration and would thus provide no reliable basis to set up normal compaction trends and maximum burial depth estimates. The integrated analysis of porosity, bulk density, P-wave velocity, and VR measurements that are related to calibrated depth trends, however, provides rather uniform estimates for the maximum amount of sediment overburden in concert with other studies. Quantifications of eroded sediment thicknesses and maximum overburden in turn will help to improve the understanding of Upper Jurassic diagenetic conditions and reservoir properties. In terms of equivalent maximum burial depths, Franconian Alb Malm strata can be considered ideal outcrop analogues for Malm thermal water aquifers in the Munich–Moosburg–Landshut area of the NAFB.

Appendix A

Table A1. Calculated mean burial depth results (incl. standard deviation) derived from the correlation between the normal compaction trend (NCT) after Drews et al. (2018) and calculated ($v_{P_{calc}}$ derived from $Ø_{calc}$ and $v_{P_{calc\text{-}Hg}}$ derived from $Ø_{Hg}$) as well as measured P-wave velocities v_P (from borehole geophone measurements $v_{P_{geo}}$ for B05 and B10 – Buness and Bram, 2001, sonic log data $v_{P_{log}}$ for Zd – Welz, 1994, and seismic refraction survey $v_{P_{seis}}$). Additionally, the burial depth results from the correlation between the VR depth trend and measured VR are listed. From these results, the amount of removed post-Jurassic (post-Jur) sediments was also estimated. In the case of buried samples for which the mean burial depth is not equal to the total amount of eroded sediments, the amount of total sediment removal was additionally calculated. Values smaller than zero are excluded as they indicate unrealistically low burial depths, meaning that these samples were deposited later than the Middle Jurassic, although they are pre-Upper Jurassic sediments. Location abbreviations and associated locations and sampled stratigraphic units are listed and illustrated in Fig. 1.

		Method used for depth calculation (in m)			
Location	Calculated depths (m)	$v_{P_{calc}}$	$v_{P_{calc\text{-}Hg}}$	v_P	VR
B05	Mean sample burial depth	–	–	1145	–
	Total post-Jur thickness	–	–	218	–
B10	Mean sample burial depth	–	–	856	–
	Total post-Jur thickness	–	–	401	–
Db	Mean sample burial depth	1578 ± 367	2861 ± 310	–	1971 ± 70
	Total sediment removal	1571 ± 367	2854 ± 308	–	1957 ± 60
	Total post-Jur thickness	971 ± 363	2254 ± 308	–	1357 ± 60
Gh	Mean sample burial depth	2486 ± 85	4038 ± 119	–	1994
	Total post-Jur thickness	1886 ± 85	3438 ± 119	–	1393
Ha	Mean sample burial depth	1675	2704	–	1451 ± 12
	Total post-Jur thickness	1075	2103	–	850 ± 12
Itt	Mean sample burial depth	2100 ± 153	3207 ± 117	–	–
	Total sediment removal	2079 ± 153	3186 ± 117	–	–
	Total post-Jur thickness	1479 ± 153	2586 ± 117	–	–
Kr	Mean sample burial depth	1732	2677	–	2133
	Total post-Jur thickness	1132	2077	–	1533
Ms	Mean sample burial depth	967	1940	–	–
	Total post-Jur thickness	366	1339	–	–
Mg Core	Mean sample burial depth	1880 ± 159	2837 ± 132	–	1023 ± 185
	Total sediment removal	1873 ± 158	2831 ± 131	–	1019 ± 183
	Total post-Jur thickness	1273 ± 158	2231 ± 131	–	419 ± 183
Mg Pit	Mean sample burial depth	976	1861	–	1000
	Total post-Jur thickness	375	1261	–	400
Rs	Mean sample burial depth	1960	2801	–	–
	Total post-Jur thickness	1355	2196	–	–
Seismic refraction survey	Mean sample burial depth	–	–	793 ± 372	–
	Total sediment removal	–	–	765 ± 380	–
	Total post-Jur thickness	–	–	–	–
Sl	Mean sample burial depth	1701 ± 15	2920 ± 55	–	2179
	Total post-Jur thickness	1101 ± 15	2320 ± 55	–	1579
St	Mean sample burial depth	1326 ± 99	2228 ± 31	–	2040
	Total post-Jur thickness	726 ± 99	1627 ± 31	–	1440
Us	Mean sample burial depth	2420 ± 186	3513 ± 558	–	1670
	Total post-Jur thickness	1820 ± 186	2913 ± 558	–	1070
Vb	Mean sample burial depth	1484 ± 244	2486 ± 590	–	–
	Total sediment removal	1443 ± 240	2445 ± 584	–	–
	Total post-Jur thickness	843 ± 240	1845 ± 584	–	–
Zg	Mean sample burial depth	1960 ± 445	2948 ± 1057	–	–
	Total sediment removal	1905 ± 446	2894 ± 1057	–	–
	Total post-Jur thickness	1305 ± 446	2294 ± 1057	–	–
Zd	Mean sample burial depth	–	–	1044 ± 394	–
	Total sediment removal	–	–	1021 ± 395	–
	Total post-Jur thickness	–	–	261 ± 395	–
All	Mean sample burial depth	1796 ± 448	2839 ± 812	931 ± 393	1659 ± 443
	Total post-Jur thickness	1163 ± 446	2206 ± 812	162 ± 416	1056 ± 442

Table A2. Supplementary table of all measurement results. Italic numbers represent values that are calculated from measurement results. Abbreviations are as follows. TVD: true vertical depth; GSF: grain size fraction; VR: vitrinite reflectance; XRD: X-ray diffraction; Acc. min.: accessory minerals; N.s.a.: northern study area; Cs. P.: claystone pit; B. g.: borehole geophone; S.s.: seismic survey.

Sample ID	Location	Sample type	Coordinates (±10 m)		TVD	ρ_{b_dry}	ρ_t	Φ_{Hg}	Φ_{calc}	v_P	$v_{P_{calc\text{-}Hg}}$	$v_{P_{calc}}$	GSF			VR	XRD		
													< 2 µm	2–63 µm	> 63 µm		Clay minerals	$CaCO_3$	Acc. min.
			X	Y	m	g cm^{-3}	g cm^{-3}	%	%	m s^{-1}	m s^{-1}	m s^{-1}	%	%	%	% Ro	wt %	wt %	wt %
US1-1b	Unterstürmig	Cs. P.	4 431 270	5 517 510	0.50	2.37	2.70	7.25	*13.40*	–	*4389*	*3826*	–	–	–	0.50	–	–	–
US1-2c	Unterstürmig	Cs. P.	4 431 270	5 517 510	0.50	2.31	2.71	11.58	*15.67*	–	*3989*	*3628*	–	–	–	–	–	–	–
ST1-T	Sengenthal	Cs. P.	4 461 882	5 455 676	0.50	2.08	2.68	15.92	*23.91*	–	*3607*	*2945*	–	–	–	–	–	–	–
ST2-T	Sengenthal	Cs. P.	4 461 882	5 455 676	0.50	2.13	2.76	15.51	*22.00*	–	*3642*	*3104*	10.47	40.35	49.17	–	33.8	11.5	54.2
RS1	Reichenschwand	Cs. P.	4 455 450	5 486 790	0.50	2.25	2.69	12.35	*17.58*	–	*3920*	*3466*	2.53	50.61	46.85	–	53.8	5.3	39.9
GH1	Großheirath	Cs. P.	4 425 662	5 560 960	0.50	2.34	2.69	7.73	*14.61*	–	*4344*	*3720*	2.61	30.38	67.01	0.57	–	–	–
GH2-1	Großheirath	Cs. P.	4 425 662	5 560 960	0.50	2.36	2.76	6.99	*13.61*	–	*4413*	*3808*	5.72	30.90	63.37	–	–	–	–
MG1	Mistelgau	Cs. P.	4 461 603	5 529 789	0.50	2.01	2.72	18.32	*26.56*	–	*3404*	*2752*	7.87	19.85	72.28	0.36	49.9	20.4	28.7
SL-H1	Schönlind	Cs. P.	4 483 436	5 493 298	0.50	2.20	2.85	12.02	*19.47*	–	*3949*	*3309*	2.28	53.88	43.84	0.61	–	–	–
SL-S2	Schönlind	Cs. P.	4 483 436	5 493 298	0.50	2.20	2.69	11.48	*19.72*	–	*3998*	*3288*	4.20	49.69	46.11	–	–	–	–
HH1-T	Hartmannshof	Cs. P.	4 468 009	5 485 046	0.50	2.19	2.75	12.87	*19.81*	–	*3873*	*3281*	8.86	39.15	52.00	–	32.8	37.5	57.7
HH1-K	Hartmannshof	Cs. P.	4 468 009	5 485 046	0.50	–	–	–	–	–	–	–	–	–	–	0.45	–	–	–
HH2-K	Hartmannshof	Cs. P.	4 468 009	5 485 046	0.50	–	–	–	–	–	–	–	–	–	–	0.46	–	–	–
MS	Marloffstein	Cs. P.	4 432 488	5 498 710	0.50	2.01	2.67	17.73	*26.67*	–	*3454*	*2744*	1.41	47.31	51.28	–	54.9	6.7	37.6
Kr	Kalchreuth	Cs. P.	4 437 792	5 489 800	0.50	2.21	2.69	13.01	*19.34*	–	*3861*	*3319*	0.95	49.16	49.89	0.60	–	–	–
ZS26_1	Zankschlag	Core	4 463 112	5 476 029	49.65	2.34	–	9.86	*14.34*	–	*4145*	*3744*	3.98	31.74	64.28	–	–	–	–
ZS26_2	Zankschlag	Core	4 463 112	5 476 029	50.00	–	–	–	–	–	–	–	26.32	40.44	33.24	–	16.1	63.3	20.2
ZS26_3	Zankschlag	Core	4 463 112	5 476 029	50.40	2.49	–	3.26	*8.94*	–	*4775*	*4231*	5.81	42.33	51.87	–	–	–	–
ZS26_4	Zankschlag	Core	4 463 112	5 476 029	50.95	2.20	–	14.22	*19.72*	–	*3754*	*3288*	7.08	42.39	50.53	–	–	–	–
ZS26_5	Zankschlag	Core	4 463 112	5 476 029	51.30	2.19	–	14.02	*19.90*	–	*3772*	*3274*	7.68	40.81	51.52	–	–	–	–
ZS26_6	Zankschlag	Core	4 463 112	5 476 029	51.70	2.20	–	13.49	*19.38*	–	*3818*	*3316*	6.78	41.14	52.08	–	–	–	–
ZS26_7	Zankschlag	Core	4 463 112	5 476 029	52.10	2.19	2.69	14.57	*19.88*	–	*3724*	*3275*	7.18	43.22	49.60	–	–	–	–
ZS26_8	Zankschlag	Core	4 463 112	5 476 029	52.60	2.24	–	12.02	*17.97*	–	*3949*	*3434*	2.45	55.92	41.63	–	–	–	–
ZS26_9	Zankschlag	Core	4 463 112	5 476 029	52.80	2.28	2.75	12.19	*16.68*	–	*3934*	*3542*	4.03	55.02	40.95	–	–	–	–
ZS26_10	Zankschlag	Core	4 463 112	5 476 029	53.00	2.24	–	11.64	*18.12*	–	*3983*	*3421*	–	–	–	–	–	–	–
ZS26_11	Zankschlag	Core	4 463 112	5 476 029	53.35	2.21	2.73	12.59	*19.20*	–	*3898*	*3331*	2.42	48.21	49.37	–	–	–	–
ZS26_12	Zankschlag	Core	4 463 112	5 476 029	53.75	2.35	–	10.80	*13.92*	–	*4059*	*3781*	13.83	53.12	33.05	–	–	–	–
ZS26_13	Zankschlag	Core	4 463 112	5 476 029	53.95	2.18	–	13.71	*20.19*	–	*3799*	*3250*	5.28	3.52	91.20	–	–	–	–
ZS26_14	Zankschlag	Core	4 463 112	5 476 029	54.15	2.21	2.72	13.17	*19.22*	–	*3847*	*3329*	0.50	44.24	55.26	–	–	–	–
ZS26_15	Zankschlag	Core	4 463 112	5 476 029	54.55	2.39	–	9.62	*12.53*	–	*4168*	*3904*	9.43	39.88	50.70	–	–	–	–
ZS26_16	Zankschlag	Core	4 463 112	5 476 029	55.05	2.24	–	13.35	*18.11*	–	*3831*	*3422*	3.90	55.01	41.10	–	–	–	–
ZS26_17	Zankschlag	Core	4 463 112	5 476 029	55.44	2.30	2.85	12.33	*15.74*	–	*3922*	*3622*	4.20	48.18	47.62	–	–	–	–
ZS26_18	Zankschlag	Core	4 463 112	5 476 029	55.80	2.22	–	14.23	*18.84*	–	*3754*	*3361*	7.57	31.68	60.75	–	–	–	–
ZS26_19	Zankschlag	Core	4 463 112	5 476 029	56.96	2.18	–	13.06	*20.39*	–	*3856*	*3234*	0.70	2.20	97.10	–	–	–	–
ZS26_20	Zankschlag	Core	4 463 112	5 476 029	57.06	2.19	–	1.40	*19.85*	–	*4960*	*3277*	2.59	2.27	95.13	–	–	–	–
ZS26_22	Zankschlag	Core	4 463 112	5 476 029	57.36	2.20	2.77	17.54	*19.62*	–	*3469*	*3296*	7.14	44.49	48.37	–	–	–	–
ZS26_23	Zankschlag	Core	4 463 112	5 476 029	57.90	2.23	2.71	13.26	*18.48*	–	*3838*	*3390*	2.15	42.62	55.23	–	–	–	–
ZS26_24	Zankschlag	Core	4 463 112	5 476 029	58.16	2.20	–	14.10	*19.68*	–	*3765*	*3291*	4.71	26.61	68.67	–	–	–	–
ZS26_25	Zankschlag	Core	4 463 112	5 476 029	58.60	2.18	2.73	15.49	*20.46*	–	*3644*	*3228*	–	–	–	–	–	–	–
ZS26_26	Zankschlag	Core	4 463 112	5 476 029	58.98	2.18	–	14.05	*20.12*	–	*3769*	*3256*	–	–	–	–	–	–	–
ZS26_27	Zankschlag	Core	4 463 112	5 476 029	58.14	–	–	–	–	–	–	–	3.48	41.16	55.35	–	–	–	–
ZS26_29	Zankschlag	Core	4 463 112	5 476 029	56.85	–	–	–	–	–	–	–	5.41	54.01	40.58	–	–	–	–
ZS26_30	Zankschlag	Core	4 463 112	5 476 029	56.02	–	–	–	–	–	–	–	1.50	19.15	79.34	–	–	–	–
ZS26_33	Zankschlag	Core	4 463 112	5 476 029	58.03	2.25	–	14.28	*17.73*	–	*3749*	*3453*	1.06	53.97	44.96	–	–	–	–

https://doi.org/10.5194/se-13-1003-2022

Table A2. Continued.

Sample ID	Location	Sample type	Coordinates (±10 m)		TVD	ρ_{b_dry}	ρ_t	Φ_{Hg}	Φ_{calc}	v_P	$v_{P_{calc\text{-}Hg}}$	$v_{P_{calc}}$	GSF			VR	XRD		
													< 2 µm	2–63 µm	> 63 µm		Clay minerals	$CaCO_3$	Acc. min.
			X	Y	m	g cm^{-3}	g cm^{-3}	%	%	m s^{-1}	m s^{-1}	m s^{-1}	%	%	%	% Ro	wt %	wt %	wt %
ZS26_34	Zankschlag	Core	4 463 112	5 476 029	61.20	2.32	–	13.85	*15.17*	–	*3787*	*3672*	–	–	–	–	–	–	–
V24_2	Velburg	Core	4 475 168	5 452 094	24.77	2.17	2.87	16.98	*20.49*	–	*3517*	*3226*	–	–	–	–	–	–	–
V24_3	Velburg	Core	4 475 168	5 452 094	46.05	2.16	2.72	14.68	*21.07*	–	*3714*	*3179*	–	–	–	–	–	-	–
V24_4	Velburg	Core	4 475 168	5 452 094	46.13	2.15	2.73	14.06	*21.29*	–	*3769*	*3161*	–	–	–	–	–	–	–
V24_5	Velburg	Core	4 475 168	5 452 094	46.17	–	–	–	–	–	–	–	1.93	37.92	60.15	–	–	–	–
V24_6	Velburg	Core	4 475 168	5 452 094	46.40	2.19	2.76	8.14	*19.98*	–	*4305*	*3267*	–	–	–	–	–	–	–
V24_7	Velburg	Core	4 475 168	5 452 094	47.54	2.16	2.73	8.38	*21.18*	–	*4283*	*3170*	–	–	–	–	–	–	–
V24_8	Velburg	Core	4 475 168	5 452 094	48.65	2.15	2.75	14.52	*21.20*	–	*3728*	*3168*	–	–	–	–	–	–	–
V24_9	Velburg	Core	4 475 168	5 452 094	47.95	2.14	2.72	14.98	*21.63*	–	*3688*	*3133*	–	–	–	–	–	–	–
V24_10	Velburg	Core	4 475 168	5 452 094	48.60	2.23	–	12.92	*18.53*	–	*3869*	*3387*	–	–	–	–	–	–	–
V24_11	Velburg	Core	4 475 168	5 452 094	48.71	–	–	–	–	–	–	–	1.71	42.06	56.23	–	–	–	–
V24_12	Velburg	Core	4 475 168	5 452 094	48.02	2.03	–	15.38	*25.69*	–	*3653*	*2818*	6.28	40.54	53.18	–	–	–	–
V24_13	Velburg	Core	4 475 168	5 452 094	49.45	2.20	–	15.61	*19.57*	–	*3634*	*3300*	–	–	–	–	–	–	–
V24_14	Velburg	Core	4 475 168	5 452 094	49.95	2.19	–	13.85	*19.83*	–	*3787*	*3279*	–	–	–	–	–	–	–
V24_15	Velburg	Core	4 475 168	5 452 094	25.50	2.18	–	14.28	*20.26*	–	*3749*	*3244*	–	–	–	–	–	–	–
V24_16	Velburg	Core	4 475 168	5 452 094	25.95	2.06	–	19.57	*24.68*	–	*3301*	*2895*	–	–	–	–	–	–	–
V24_17	Velburg	Core	4 475 168	5 452 094	24.95	2.01	–	19.63	*26.67*	–	*3296*	*2744*	–	–	–	–	–	–	–
MG_3.00–3.10	Mistelgau	Core	4 461 603	5 529 789	3.04	–	–	–	–	–	–	–	–	–	–	–	26.8	39.2	33.9
MG_3.35–3.45	Mistelgau	Core	4 461 603	5 529 789	3.36	–	–	–	–	–	–	–	–	–	–	–	25.8	37.7	36.3
MG_3.47–3.55	Mistelgau	Core	4 461 603	5 529 789	3.48	–	–	–	–	–	–	–	–	–	–	–	30.1	34.1	35.8
MG_5.10–5.25	Mistelgau	Core	4 461 603	5 529 789	5.18	2.20	2.71	12.41	*19.69*	–	*3914*	*3290*	–	–	–	0.32	50.5	1.5	47.4
MG_5.25–5.60	Mistelgau	Core	4 461 603	5 529 789	5.42	2.21	2.91	13.04	*19.15*	–	*3858*	*3335*	–	–	–	–	54.0	2.4	43.0
MG_7.40–7.50	Mistelgau	Core	4 461 603	5 529 789	7.46	2.27	–	11.18	*17.04*	–	*4025*	*3512*	–	–	–	0.40	50.0	7.4	41.9
MG_7.70–7.90	Mistelgau	Core	4 461 603	5 529 789	7.62	2.27	2.72	12.12	*17.01*	–	*3940*	*3514*	–	–	–	–	–	–	–
DB_3.50	Dörlbach	Core	4 453 559	5 468 616	3.50	2.02	2.78	15.31	*26.04*	–	*3659*	*2791*	–	–	–	0.53	49.4	3.2	46.1
DB_4.00	Dörlbach	Core	4 453 559	5 468 616	4.00	–	–	–	–	–	–	–	–	–	–	–	9.1	79.1	11.2
DB_4.35	Dörlbach	Core	4 453 559	5 468 616	4.37	–	–	–	–	–	–	–	–	–	–	–	43.4	3.1	52.8
DB_4.50	Dörlbach	Core	4 453 559	5 468 616	4.53	–	–	–	–	–	–	–	–	–	–	–	42.9	13.0	43.3
DB_5.00	Dörlbach	Core	4 453 559	5 468 616	5.00	2.25	2.68	11.63	*17.88*	–	*3984*	*3441*	–	–	–	–	51.3	2.6	45.4
DB_6.00–6.15	Dörlbach	Core	4 453 559	5 468 616	6.07	2.14	2.71	12.40	*21.92*	–	*3915*	*3111*	–	–	–	–	49.2	5.7	44.5
DB_6.15–6.30	Dörlbach	Core	4 453 559	5 468 616	6.18	–	–	–	–	–	–	–	–	–	–	–	48.8	5.7	44.9
DB_6.30–6.60	Dörlbach	Core	4 453 559	5 468 616	6.42	–	–	–	–	–	–	–	–	–	–	–	51.0	3.7	44.4
DB_6.90–7.00	Dörlbach	Core	4 453 559	5 468 616	6.96	–	–	–	–	–	–	–	–	–	–	–	54.8	3.0	41.8
DB_7.00–7.20	Dörlbach	Core	4 453 559	5 468 616	7.10	–	–	–	–	–	–	–	–	–	–	–	26.0	40.2	32.7
DB_7.25–7.35	Dörlbach	Core	4 453 559	5 468 616	7.33	–	–	–	–	–	–	–	–	–	–	0.74	51.4	3.5	44.5
DB_7.90–8.00	Dörlbach	Core	4 453 559	5 468 616	7.95	2.17	2.80	12.56	*20.54*	–	*3901*	*3221*	–	–	–	–	52.4	3.0	44.2
DB_8.10–8.25	Dörlbach	Core	4 453 559	5 468 616	8.13	–	–	–	–	–	–	–	–	–	–	–	54.2	3.1	42.1
DB_8.75–8.90	Dörlbach	Core	4 453 559	5 468 616	8.80	–	–	–	–	–	–	–	–	–	–	–	53.4	3.4	42.4
DB_9.00–9.15	Dörlbach	Core	4 453 559	5 468 616	9.05	–	–	–	–	–	–	–	–	–	–	–	51.9	3.3	44.3
DB_9.25–9.35	Dörlbach	Core	4 453 559	5 468 616	9.30	2.29	2.69	10.16	*16.29*	–	*4118*	*3575*	–	–	–	–	51.8	4.2	43.4
DB_9.55–9.70	Dörlbach	Core	4 453 559	5 468 616	9.63	–	–	–	–	–	–	–	–	–	–	–	53.9	3.9	41.6
DB_10.00	Dörlbach	Core	4 453 559	5 468 616	10.02	–	–	–	–	–	–	–	–	–	–	–	51.9	3.3	44.5
DB_10.35	Dörlbach	Core	4 453 559	5 468 616	10.35	2.12	2.77	10.86	*22.60*	–	*4054*	*3056*	–	–	–	–	53.2	3.0	43.2
DB_10.45	Dörlbach	Core	4 453 559	5 468 616	10.45	–	–	–	-	–	–	–	–	–	–	–	52.8	4.0	42.8
Itt_V87_20.45	Ittling	Core	4 455 389	5 498 496	20.45	–	–	–	–	–	–	–	–	–	–	–	34.3	31.3	33.8
Itt_V87_20.80	Ittling	Core	4 455 389	5 498 496	20.80	2.25	2.69	11.25	*17.74*	–	*4019*	*3453*	–	–	–	–	–	–	–

Table A2. Continued.

Sample ID	Location	Sample type	Coordinates (±10 m)		TVD	ρ_{b_dry}	ρ_t	Φ_{Hg}	Φ_{calc}	v_P	$v_{P_{calc\text{-}Hg}}$	$v_{P_{calc}}$	GSF			VR	XRD		
													< 2 µm	2–63 µm	> 63 µm		Clay minerals	$CaCO_3$	Acc. min.
			X	Y	m	g cm^{-3}	g cm^{-3}	%	%	m s^{-1}	m s^{-1}	m s^{-1}	%	%	%	% Ro	wt %	wt %	wt %
Itt_V87_21.00	Ittling	Core	4 455 389	5 498 496	21.00	2.27	2.69	10.18	*17.05*	–	*4116*	*3511*	–	–	–	–	37.4	7.7	54.5
Itt_V87_21.04	Ittling	Core	4 455 389	5 498 496	21.04	2.28	2.65	9.84	*16.73*	–	*4147*	*3538*	–	–	–	–	33.4	7.8	58.0
Itt_V87_21.38	Ittling	Core	4 455 389	5 498 496	21.38	–	–	–	–	–	–	–	–	–	–	–	42.4	10.7	46.0
Itt_V87_21.51	Ittling	Core	4 455 389	5 498 496	21.51	2.33	2.71	10.47	*14.92*	–	*4090*	*3693*	–	–	–	–	–	–	–
Itt_V87_21.80	Ittling	Core	4 455 389	5 498 496	21.80	–	–	–	–	–	–	–	–	–	–	–	41.6	9.5	48.6
B05	Eichstätt	B. g.	4 442 241	5 415 335	327.00	–	–	–	–	2890	–	–	–	–	–	–	–	–	–
B10	Daiting	B. g.	4 418 359	5 406 274	455.00	–	–	–	–	2650	–	–	–	–	–	–	–	–	–
4/85	Zapfendorf	Sonic Log	4 429 110	5 542 650	15.80	–	–	–	–	2890	–	–	–	–	–	–	–	–	–
4/85	Zapfendorf	Sonic Log	4 429 110	5 542 650	16.50	–	–	–	–	2725	–	–	–	–	–	–	–	–	–
4/85	Zapfendorf	Sonic Log	4 429 110	5 542 650	17.00	–	–	–	–	2681	–	–	–	–	–	–	–	–	–
4/85	Zapfendorf	Sonic Log	4 429 110	5 542 650	18.80	–	–	–	–	2770	–	–	–	–	–	–	–	–	–
4/85	Zapfendorf	Sonic Log	4 429 110	5 542 650	19.80	–	–	–	–	2841	–	–	–	–	–	–	–	–	–
4/85	Zapfendorf	Sonic Log	4 429 110	5 542 650	20.90	–	–	–	–	2604	–	–	–	–	–	–	–	–	–
4/85	Zapfendorf	Sonic Log	4 429 110	5 542 650	21.60	–	–	–	–	3125	–	–	–	–	–	–	–	–	–
4/85	Zapfendorf	Sonic Log	4 429 110	5 542 650	22.10	–	–	–	–	3115	–	–	–	–	–	–	–	–	–
4/85	Zapfendorf	Sonic Log	4 429 110	5 542 650	22.50	–	–	–	–	3205	–	–	–	–	–	–	–	–	–
4/85	Zapfendorf	Sonic Log	4 429 110	5 542 650	23.10	–	–	–	–	3356	–	–	–	–	–	–	–	–	–
4/85	Zapfendorf	Sonic Log	4 429 110	5 542 650	24.10	–	–	–	–	3300	–	–	–	–	–	–	–	–	–
4/85	Zapfendorf	Sonic Log	4 429 110	5 542 650	25.80	–	–	–	–	2584	–	–	–	–	–	–	–	–	–
4/85	Zapfendorf	Sonic Log	4 429 110	5 542 650	26.40	–	–	–	–	2525	–	–	–	–	–	–	–	–	–
4/85	Zapfendorf	Sonic Log	4 429 110	5 542 650	26.80	–	–	–	–	2500	–	–	–	–	–	–	–	–	–
4/85	Zapfendorf	Sonic Log	4 429 110	5 542 650	27.40	–	–	–	–	2433	–	–	–	–	–	–	–	–	–
4/85	Zapfendorf	Sonic Log	4 429 110	5 542 650	28.00	–	–	–	–	2392	–	–	–	–	–	–	–	–	–
4/85	Zapfendorf	Sonic Log	4 429 110	5 542 650	29.00	–	–	–	–	2392	–	–	–	–	–	–	–	–	–
162	N.s.a.	S.s.	4 462 717	5 526 786	17.88	–	–	–	–	2433	–	–	–	–	–	–	–	–	–
158	N.s.a.	S.s.	4 459 517	5 529 194	20.68	–	–	–	–	3354	–	–	–	–	–	–	–	–	–
157	N.s.a.	S.s.	4 458 397	5 529 759	21.98	–	–	–	–	2883	–	–	–	–	–	–	–	–	–
155	N.s.a.	S.s.	4 456 657	5 530 941	87.41	–	–	–	–	2203	–	–	–	–	–	–	–	–	–
168	N.s.a.	S.s.	4 467 573	5 523 752	38.59	–	–	–	–	2215	–	–	–	–	–	–	–	–	–
80	N.s.a.	S.s.	4 425 179	5 552 622	22.56	–	–	–	–	2935	–	–	–	–	–	–	–	–	–
83	N.s.a.	S.s.	4 427 645	5 554 515	20.86	–	–	–	–	2665	–	–	–	–	–	–	–	–	–
82	N.s.a.	S.s.	4 426 750	5 553 694	22.62	–	–	–	–	2637	–	–	–	–	–	–	–	–	–
116	N.s.a.	S.s.	4 423 532	5 552 959	40.74	–	–	–	–	2493	–	–	–	–	–	–	–	–	–
78	N.s.a.	S.s.	4 423 448	5 551 656	21.63	–	–	–	–	2387	–	–	–	–	–	–	–	–	–
76	N.s.a.	S.s.	4 421 799	5 550 442	15.37	–	–	–	–	2689	–	–	–	–	–	–	–	–	–
204	N.s.a.	S.s.	4 427 396	5 541 869	19.09	–	–	–	–	2614	–	–	–	–	–	–	–	–	–
203	N.s.a.	S.s.	4 426 895	5 541 393	19.86	–	–	–	–	2292	–	–	–	–	–	–	–	–	–
224	N.s.a.	S.s.	4 444 097	5 554 516	39.15	–	–	–	–	2185	–	–	–	–	–	–	–	–	–
232	N.s.a.	S.s.	4 450 911	5 559 442	21.79	–	–	–	–	2724	–	–	–	–	–	–	–	–	–

Data availability. All datasets that were used are either indicated by references in the Data section (Buness and Bram, 2001; Welz, 1994) or listed in Table A2 in the Appendix.

Author contributions. SF was responsible for the organization of the drilling and coring campaign as well as the sampling, acquisition of published data, subsequent sample preparation, petrophysical measurements (density and porosity), data analysis, and interpretation. He was also primarily responsible for drafting and writing this work. MD coordinated this study and significantly contributed to the data analysis, interpretation, drafting, and structuring of this work. WB helped with the management of administrative procedures regarding the drilling and coring campaign, the acquisition of the seismic refraction data in northern Bavaria, and also improving the quality of this work by revising the paper. FD prepared the inset figure in Fig. 1 and provided valuable input regarding the correct and thorough description of the regional geological history. DM provided the VR reference data for the VR depth trend from the NAFB, conducted the measurements of the vitrinite reflectance, and substantially contributed to their interpretation. HS significantly contributed by thoroughly revising, reworking, and structuring this work.

Competing interests. The contact author has declared that neither they nor their co-authors have any competing interests.

Disclaimer. Publisher's note: Copernicus Publications remains neutral with regard to jurisdictional claims in published maps and institutional affiliations.

Acknowledgements. We are grateful that the Autobahndirektion Nordbayern (Sibylle Glück) provided us with cores from various locations, and we are also grateful to the TUM hydrogeology group headed by Florian Einsiedl and to the head of the Geoth. Energ. group led by Kai Zosseder, in particular to Daniel Bohnsack for providing us with access to their helium pycnometer. We would also like to thank Reinhard Sachsenhofer for valuable input on the regional geology of the North Alpine Foreland Basin and existing thermal maturity data. The work of David Misch was supported by the Austrian Science Fund FWF (grant no.: P 33883-N). For conducting the grain size distribution measurements, we thank Ute Schmidt from the Institute of Geography at FAU. Many thanks are also directed to Heinz Meyer (mayor of Burgthann) and Karl Lappe (mayor of Mistelgau), who supported the realization of this study by authorizing the drilling on their estates. We are also grateful for the very helpful comments by Hilmar von Eynatten and Thomas Voigt as well as for the critical constructive review and suggestions that helped to improve the final version of the paper.

Financial support. This research has been supported by the Bayerisches Staatsministerium für Wissenschaft, Forschung und Kunst (grant no. not applicable).

Review statement. This paper was edited by Kei Ogata and reviewed by Thomas Voigt and Hilmar von Eynatten.

References

Aplin, A. C., Matenaar, I. F., McCarty, D. K., and van der Pluijm, B. A.: Influence of mechanical compaction and clay mineral diagenesis on the microfabric and pore-scale properties of deep-water Gulf of Mexico mudstones, Clay. Clay Miner., 54, 500–514, 2006.

Athy, L. F.: Density, Porosity, and Compaction of Sedimentary Rocks, AAPG Bull., 14, 1–24, 1930.

Bachmann, G. H. and Müller, M.: Sedimentary and structural evolution of the German Molasse Basin, Eclogae Geol. Helv., 85, 519–530, https://doi.org/10.5169/SEALS-167019, 1992.

Bachmann, G. H., Müller, M., and Weggen, K.: Evolution of the Molasse Basin (Germany, Switzerland), Tectonophysics, 137, 77–92, 1987.

Bachmann, G. H., Hiltmann, W., and Lerche, I.: Inkohlung des Unteren Keupers in Südwestdeutschland, N. Jb. Geol. Paläont. Abh., 226, 271–288, 2002.

Bader, K.: Der Grundgebirgsrücken in Mittelfranken (südlich von Nürnberg) nach refraktionsseismischen Messungen, Geologisches Jahrbuch, 58, 7–33, 2001.

Baig, I., Faleide, J. I., Mondol, N. H., and Jahren, J.: Burial and exhumation history controls on shale compaction and thermal maturity along the Norwegian North Sea basin margin areas, Mar. Petrol. Geol., 104, 61–85, https://doi.org/10.1016/j.marpetgeo.2019.03.010, 2019.

Baran, R., Friedrich, A. M., and Schlunegger, F.: The late Miocene to Holocene erosion pattern of the Alpine foreland basin reflects Eurasian slab unloading beneath the western Alps rather than global climate change, Lithosphere, 6, 124–131, https://doi.org/10.1130/L307.1, 2014.

Bauer, W.: Geothermische Verhältnisse des Fränkischen Beckens, Julius-Maximilians-Universität, Würzburg, ISSN 09309-3757, 2000.

Bjørlykke, K.: Principal aspects of compaction and fluid flow in mudstones, in: Muds and mudstones: physical and fluid-flow properties, vol. 158, edited by: Aplin, A. C., Fleet, A. J., and Macquaker, J. H. S., Geological Society of London, 73–78, 1999.

Bjørlykke, K.: Petroleum Geoscience, 2nd ed., Springer Berlin Heidelberg, Oslo, ISBN 978-3-642-34131-1, https://doi.org/10.1007/978-3-642-34132-8, 2015.

Bohnsack, D., Potten, M., Pfrang, D., Wolpert, P., and Zosseder, K.: Porosity–permeability relationship derived from Upper Jurassic carbonate rock cores to assess the regional hydraulic matrix properties of the Malm reservoir in the South German Molasse Basin, Geoth. Energ., 8, 12, https://doi.org/10.1186/s40517-020-00166-9, 2020.

Bohnsack, D., Potten, M., Freitag, S., Einsiedl, F., and Zosseder, K.: Stress sensitivity of porosity and permeability under varying hydrostatic stress conditions for different carbonate rock types of the geothermal Malm reservoir in Southern Germany, Geoth. Energ., 9, 15, https://doi.org/10.1186/s40517-021-00197-w, 2021.

Buness, H.-A. and Bram, K.: Die Muschelkalkoberfläche und die permische Peneplain in Mittelfranken abgeleitet aus seismischen Messungen, Geologisches Jahrbuch, [data set], 58, 35–60, 2001.

Čermák, V. and Brodi, L.: A heat production model of the crust and upper mantle, Tectonophysics, 194, 307–323, 1991.

Commission, G. S.: Stratigraphic Table of Germany 2016, German Research Centre for Geosciences, Potsdam, ISBN 978-3-9816597-7-1, 2016.

Corcoran, D. v and Doré, A. G.: A review of techniques for the estimation of magnitude and timing of exhumation in offshore basins, Earth-Sci. Rev., 72, 129–168, https://doi.org/10.1016/j.earscirev.2005.05.003, 2005.

De Wall, H., Schaarschmidt, A., Kämmlein, M., Gabriel, G., Bestmann, M., and Scharfenberg, L.: Subsurface granites in the Franconian Basin as the source of enhanced geothermal gradients: a key study from gravity and thermal modeling of the Bayreuth Granite, Int. J. Earth Sci., 108, 1913–1936, https://doi.org/10.1007/s00531-019-01740-8, 2019.

Deutsches Institut für Normung: Baugrund und Grundwasser; Benennen und Beschreiben von Boden und Fels; Schichtenverzeichnis für Bohrungen ohne durchgehende Gewinnung von gekernten Proben im Boden und im Fels, 1987.

Dewhurst, D. N., Aplin, A. C., Sarda, J.-P., Jean-P., and Yang, Y.: Compaction-driven evolution of porosity and permeability in natural mudstones: An experimental study, J. Geophys. Res., 103, 651–661, 1998.

Dill, H.: Heavy mineral response to the progradation of an alluvial fan: implications concerning unroofing of source area, chemical weathering and palaeo-relief (Upper Cretaceous Parkstein fan complex, SE Germany), Sediment. Geol., 95, 39–56, 1995.

Drews, M. C., Bauer, W., Caracciolo, L., and Stollhofen, H.: Disequilibrium compaction overpressure in shales of the Bavarian Foreland Molasse Basin: Results and geographical distribution from velocity-based analyses, Mar. Petrol. Geol., 92, 37–50, https://doi.org/10.1016/j.marpetgeo.2018.02.017, 2018.

Drews, M. C., Hofstetter, P., Zosseder, K., Straubinger, R., Gahr, A., and Stollhofen, H.: Predictability and controlling factors of overpressure in the North Alpine Foreland Basin, SE Germany: an interdisciplinary postdrill analysis of the Geretsried GEN-1 deep geothermal well, Geoth. Energ., 8, 20, https://doi.org/10.1186/s40517-019-0121-z, 2020.

Earth Resources Observation And Science Center: Shuttle Radar Topography Mission (SRTM) 1 Arc-Second Global [data set], https://doi.org/10.5066/F7PR7TFT, 2017.

Eberle, J., Eitel, B., Blümel, W. D., and Wittmann, P.: Deutschlands Süden – vom Erdmittelalter zur Gegenwart, Springer Berlin Heidelberg, Berlin, Heidelberg, 203 pp., https://doi.org/10.1007/978-3-662-54381-8, 2017.

Fawad, M., Mondol, N. H., Jahren, J., and Bjørlykke, K.: Microfabric and rock properties of experimentally compressed silt-clay mixtures, Mar. Petrol. Geol., 27, 1698–1712, 2010.

Freudenberger, W. and Schwerd, K.: Erläuterungen zur Geologischen Karte von Bayern 1:500000, 4th ed., Bayerisches Geologisches Landesamt, München, 1996.

Freudenberger, W., Geyer, G., and Schröder, B.: Der Buntsandstein in Bayern (nordwestliches Franken, Bruchschollenland und Randfazies im Untergrund), in: Stratigraphie von Deutschland XI, Buntsandstein, vol. 68, edited by: Lepper, J. and Röhling, H.-G., Schweizerbart'sche Verlagsbuchhandlung, Stuttgart, 547–582, https://doi.org/10.1127/sdgg/69/2014/547, 2013.

Giles, M. R., Indrelid, S. L., and James, D. M. D.: Compaction – the great unknown in basin modelling, J. Geol. Soc. London, 141, 15–43, https://doi.org/10.1144/GSL.SP.1998.141.01.02, 1998.

Glaser, S., Lagally, U., Schenk, P., Eichhorn, R., Brandt, S., Loth, G., and Loth, R.: Geotope in Mittelfranken, 2., edited by: Glaser, S., Bayerisches Geologisches Landesamt, München, 128 pp., 2001.

Goulty, N. R.: Relationships between porosity and effective stress in shales, First Break, 413–419, 1998.

Gusterhuber, J., Dunkl, I., Hinsch, R., Linzer, H.-G., and Sachsenhofer, R. F.: Neogene uplift and erosion in the Alpine Foreland Basin (Upper Austria and Salzburg), Geol. Carpath., 63, 295–305, https://doi.org/10.2478/v10096-012-0023-5, 2012.

Hedenblad, G.: The use of mercury intrusion porosimetry or helium porosity to predict the moisture transport properties of hardened cement paste, Adv. Cem. Based Mater., 6, 123–129, https://doi.org/10.1016/S1065-7355(97)90019-5, 1997.

Hejl, E., Coyle, D. A., Lal, N., van den Haute, P., and Wagner, G. A.: Fission-track dating of the western border of the Bohemian massif – thermochronology and tectonic implications, Geol. Rundsch., 86, 210–219, 1997.

Henk, A.: Mächtigkeit und Alter der erodierten Sedimente im Saar-Nahe-Becken (SW-Deutschland), Geol. Rundsch., 81, 323–331, https://doi.org/10.1007/BF01828601, 1992.

Heppard, P. D., Cander, H. S., and Eggertson, E. B.: Abnormal Pressure and the Occurrence of Hydrocarbons in Offshore Eastern Trinidad, West Indies, AAPG Memoir., 70, 215–246, 1998.

Hertle, M. and Littke, R.: Coalification pattern and thermal modelling of the Permo-Carboniferous Saar Basin (SW-Germany), Int. J. Coal Geol., 42, 273–296, 2000.

Hillis, R. R.: Quantification of Tertiary Exhumation in the United Kingdom Southern North Sea Using Sonic Velocity Data, AAPG Bull., 79, 130–152, 1995.

Homuth, S., Götz, A. E., and Sass, I.: Lithofacies and depth dependency of thermo- and petrophysical rock parameters of the Upper Jurassic geothermal carbonate reservoirs of the Molasse Basin, Z. Dtsch. Ges. Geowiss., 165, 469–486, https://doi.org/10.1127/1860-1804/2014/0074, 2014

Horpibulsuk, S., Rachan, R., Chinkulkijniwat, A., Raksachon, Y., and Suddeepong, A.: Analysis of strength development in cement-stabilized silty clay from microstructural considerations, Construct. Build. Mater., 24, 2011–2021, https://doi.org/10.1016/j.conbuildmat.2010.03.011, 2010.

Hunt, J. M.: Petroleum Geochemistry and Geology, W. H. Freeman and Company, ISBN 0-7167-1005-6, 1979.

Issler, D. R.: A New Approach to Shale Compaction and Stratigraphic Restoration, Beaufort-Mackenzie Basin and Mackenzie Corridor, Northern Canada, AAPG Bull., 76, 1170–1189, 1992.

Jin, J., Aigner, T., Luterbacher, H. P., Bachmann, G. H., and Müller, M.: Sequence stratigraphy and depositional history in the southeastern German Molasse Basin, Mar. Petrol. Geol., 12, 929–940, 1995.

Kämmlein, M., Bauer, W., and Stollhofen, H.: The Franconian Basin thermal anomaly, SE Germany revised: New thermal conductivity and uniformly corrected temperature data, Z. Dtsch. Ges. Geowiss., 171, 21–44, https://doi.org/10.1127/zdgg/2020/0204, 2020.

Klaver, J., Desbois, G., Urai, J. L., and Littke, R.: BIB-SEM study of the pore space morphology in early mature Posidonia Shale

from the Hils area, Germany, Int. J. Coal Geol., 103, 12–25, https://doi.org/10.1016/j.coal.2012.06.012, 2012.

Klaver, J., Hemes, S., Houben, M., Desbois, G., Radi, Z., and Urai, J. L.: The connectivity of pore space in mudstones: insights from high-pressure Wood's metal injection, BIB-SEM imaging, and mercury intrusion porosimetry, Geofluids, 15, 577–591, https://doi.org/10.1111/gfl.12128, 2015.

Koch, R. and Munnecke, A.: Fazielle Entwicklung und Korrelation des Oberjura in den Bohrungen Bad Waldsee GB2 und Altensteig 1 (Süddeutschland; Molasse-Becken; Impressamergel- bis hangende Bankkalk-Formation), Geologische Blätter NO-Bayern, 66, 165–203, 2016.

Kröner, F., Koch, R., and Munnecke, A.: Aufschlussmodelle zur Fazies-Interpretation des Oberjura im östlichen Molasse-Becken (Workshop und Exkursion; 7. und 8. August 2017; Erlangen), Geologische Blätter NO-Bayern, 67, 167–208, 2017.

Krumm, H.: Mineralbestand und Genese fränkischer Keuper- und Lias-Tone, Beiträge zur Mineralogie und Petrographie, 11, 91–137, 1965.

Krus, M., Hansen, K. K., and Künzel, H. M.: Porosity and liquid absorption of cement paste, Mater. Struct., 30, 394–398, 1997.

Kuhlemann, J. and Kempf, O.: Post-Eocene evolution of the North Alpine Foreland Basin and its response to Alpine tectonics, Sediment. Geol., 152, 45–78, https://doi.org/10.1016/S0037-0738(01)00285-8, 2002.

Le Bayon, R., Brey, G. P., Ernst, W. G., and Mählmann, R. F.: Experimental kinetic study of organic matter maturation: Time and pressure effects on vitrinite reflectance at 400 °C, Org. Geochem., 42, 340–355, https://doi.org/10.1016/j.orggeochem.2011.01.011, 2011.

Lindholm, R. C.: A practical approach to sedimentology, Springer Science & Business Media, ISBN 978-94-011-7685-9, https://doi.org/10.1007/978-94-011-7683-5, 2012.

Liu, B., Teng, J., Mastalerz, M., and Schieber, J.: Assessing the thermal maturity of black shales using vitrinite reflectance: Insights from Devonian black shales in the eastern United States, Int. J. Coal Geol., 220, 1–10, https://doi.org/10.1016/j.coal.2020.103426, 2020.

Lützner, H. and Kowalczyk, G.: Paläogeographie und Beckengliederung, Schriftenreihe der Deutschen Gesellschaft für Geowissenschaften, 61, 58–70, https://doi.org/10.1127/sdgg/61/2012/58, 2012.

Marion, D., Nur, A., Yin, H., and Han, D.: Compressional Velocity and porosity in Sand-Clay-Mixtures, Geophysics, 57, 554–563, 1992.

Mavromatidis, A. and Hillis, R. R.: Quantification of exhumation in the Eromanga Basin and its implications for hydrocarbon exploration, Petrol. Geosci., 11, 79–92, 2005.

Menpes, R. J. and Hillis, R. R.: Quantification of Tertiary exhumation from sonic velocity data, Celtic Sea/South-Western Approaches, J. Geol. Soc. London, 191–207, 1995.

Meyer, R. K. F.: Kreide nördlich der Alpen, in: Erläuterungen zur Geologischen Karte 1 : 500 000 Bayern, edited by: Landesamt, B. g., Bayerisches Geologisches Landesamt, München, 68–78, 1981.

Meyer, R. K. F.: Die Entwicklung der Pfahl-Störungszone und des Bodenwöhrer Halbgrabens auf Blatt Wackersdorf, Erlanger geologische Abhandlungen, 117, 1–24, 1989a.

Meyer, R. K. F.: Die Entwicklung der Kreide-Sedimente im Westteil der Bodenwöhrer Senke, Erlanger geologische Abhandlungen, 117, 53–90, 1989b.

Meyer, R. K. F.: Kreide, in: Erläuterungen zur Geologischen Karte 1 : 500 000 Bayern, edited by: Landesamt, B. g., Bayerisches Geologisches Landesamt, München, 112–128, 1996.

Meyer, R. K. F. and Schmidt-Kaler, H.: Paläogeographie und Schwammriffentwicklung des süddeutschen Malm – ein Überblick, Facies, 23, 175–184, https://doi.org/10.1007/BF02536712, 1990.

Meyer, R. K. F. and Schmidt-Kaler, H.: Jura, in: Erläuterungen zur Geologischen Karte 1 : 500 000 Bayern, edited by: Landesamt, B. g., Bayerisches Geologisches Landesamt, München, 90–112, 1996.

Mondol, N. H., Bjørlykke, K., Jahren, J., and Høeg, K.: Experimental mechanical compaction of clay mineral aggregates – Changes in physical properties of mudstones during burial, Mar. Petrol. Geol., 24, 289–311, https://doi.org/10.1016/j.marpetgeo.2007.03.006, 2007.

Mondol, N. H., Bjørlykke, K., and Jahren, J.: Experimental compaction of clays: relationship between permeability and petrophysical properties in mudstones, Petrol. Geosci., 14, 319–337, https://doi.org/10.1144/1354-079308-773, 2008.

Mraz, E., Moeck, I., Bissmann, S., and Hild, S.: Multiphase fossil normal faults as geothermal exploration targets in the Western Bavarian Molasse Basin: Case study Mauerstetten, Z. Dtsch. Ges. Geowiss., 169, 389–411, https://doi.org/10.1127/zdgg/2018/0166, 2018.

Nachtmann, W. and Wagner, L.: Mesozoic and Early Tertiary evolution of the Alpine foreland in upper Austria and Salzburg, Austria, Tectonophysics, 137, 61–76, https://doi.org/10.1016/0040-1951(87)90314-3, 1987.

Niebuhr, B., Pürner, T., and Wilmsen, M.: Lithostratigraphie der außeralpinen Kreide Bayerns, Schriftenreihe der Deutschen Gesellschaft für Geowissenschaften (SDGG), 65, 7–58, 2009.

Niebuhr, B., Wilmsen, M., Chellouche, P., Richardt, N., and Pürner, T.:Stratigraphy and facies of the Turonian (Upper Cretaceous) Roding Formation at the southwestern margin of the Bohemian Massif (Southern Germany, Bavaria), Z. Dtsch. Ges. Geowiss., 162, 295–316, https://doi.org/10.1127/1860-1804/2011/0162-0295, 2011.

Niebuhr, B., Richardt, N., and Wilmsen, M.: Facies and integrated stratigraphy of the Upper Turonian (Upper Cretaceous) Großberg Formation south of Regensburg (Bavaria, southern Germany), Acta Geol. Pol., 62, 595–615, https://doi.org/10.2478/v10263-012-0032-9, 2012.

Nöth, S., Karg, H., and Littke, R.: Reconstruction of Late Paleozoic heat flows and burial histories at the Rhenohercynian-Subvariscan boundary, Germany, Int. J. Earth Sci., 90, 234–256, https://doi.org/10.1007/s005310000114, 2001.

Peterek, A. and Schröder, B.: Geomorphologic evolution of the cuesta landscapes around the Northern Franconian Alb – review and synthesis, Z. Geomorphol., 54, 305–345, https://doi.org/10.1127/0372-8854/2010/0054-0037, 2010.

Peterek, A., Rauche, H., and Schröder, B.: Die strukturelle Entwicklung des E-Randes der Süddeutschen Scholle in der Kreide, Z. Geol. Wissenschaft., 24, 65–77, 1996.

Peterek, A., Rauche, H., Schröder, B., Franzke, H.-J., Bankwitz, P., and Bankwitz, E.: The late- and post-Variscan tectonic evolution

of the Western Border fault zone of the Bohemian massif, Geol. Rundsch., 86, 191–202, 1997.

Pharaoh, T. C., Dusar, M., Geluk, M. C., Kockel, F., Krawczyk, C. M., Krzywiec, P., Scheck-Wenderoth, M., Thybo, H., Vejbæk, O. v, and van Wees, J. D.: Tectonic evolution, in: Petroleum geological atlas of the Southern Permian Basin Area, edited by: Doornenbal, H. and Stevenson, A., TNO Geological Survey of the Netherlands, Utrecht; Houten the Netherlands, 25–57, 2010.

Piénkowski, G., Schudack, M. E., Bosák, P., Enay, R., Feldman-Olszewska, A., Golonka, J., Gutowski, J., Herngreen, G. F. W., Jordan, P., Krobicki, M., Lathuiliere, B., Leinfelder, R. R., Michalík, J., Mönnig, E., Noe-Nygaard, N., Pálfy, J., Pint, A., Rasser, M. W., Reisdorf, A. G., Schmid, D. U., Schweigert, G., Surlyk, F., Wetzel, A., and Wong, T. E.: Jurassic, in: The Geology of Central Europe, Mesozoic and Cenozoic, Vol. 2, edited by: McCann, T., Geol. Soc. Lond., 823–922, 2008.

Potter, P. E., Maynard, J. B., and Pryor, W. A.: Sedimentology of Shale, 1 Edn., Springer-Verlag New York Inc., 326 pp., 1980.

Przybycin, A. M., Scheck-Wenderoth, M., and Schneider, M.: Assessment of the isostatic state and the load distribution of the European Molasse basin by means of lithospheric-scale 3D structural and 3D gravity modelling, Int. J. Earth Sci., 104, 1405–1424, https://doi.org/10.1007/s00531-014-1132-4, 2015.

Raiga-Clemenceau, J., Martin, J. P., and Nicoletis, S.: The concept of acoustic formation factor for more accurate porosity determination from sonic transit time data, SPWLA 27th Annual Logging Symposium, 1986.

Reicherter, K., Froitzheim, N., Jarosiński, M., Badura, J., Franzke, H.-J., Hansen, M., Hübscher, C., müller, R., Poprawa, P., Reinecker, J., Stackebrandt, W., Voigt, T., von Eynatten, H., and Zuchiewicz, W.: Alpine tectonics north of the Alps, in: The Geology of Central Europe, Volume 2: Mesozoic and Cenozoic, edited by: McCann, T., Geol. Soc. Lond., 1233–1286, 2008.

Rubey, W. W. and Hubbert, M. K.: Role of fluid pressure in mechanics of overthrust faulting: II. Overthrust belt in geosynclinal area of western Wyoming in light of fluid-pressure hypothesis, Geol. Soc. Am. Bull., 70, 167–206, 1959.

Sachsenhofer, R. F.: Syn- and post-collisional heat flow in the Cenozoic Eastern Alps, Int. J. Earth Sci., 90, 579–592, https://doi.org/10.1007/s005310000179, 2001.

Scheck-Wenderoth, M., Krzywiec, P., Zühlke, R., Maystrenko, Y., and Froitzheim, N.: Permian to Cretaceous tectonics, in: The Geology of Central Europe, Volume 2: Mesozoic and Cenozoic, edited by: McCann, T., Geol. Soc. Lond., 2, 999–1030, 2008.

Schirmer, W.: Wortgeschichte "Kallmünzer" als Gestein, Geologische Blätter NO-Bayern, 65, 221–244, 2015.

Schröder, B.: Zur Morphogenese im Ostteil der Süddeutschen Scholle, Geol. Rundsch., 58, 10–32, 1968.

Schröder, B.: Fränkische Schweiz und Vorland, Sammlung Geologischer Führer, 86, ISBN 3443150047, 1970.

Schröder, B.: Inversion tectonics along the western margin of the Bohemian Massif, Tectonophysics, 137, 93–100, 1987.

Schröder, B., Ahrendt, H., Peterek, A., and Wemmer, K.: Post-Variscan sedimentary record of the SW margin of the Bohemian massif: a review, Geol. Rundsch., 86, 178–184, https://doi.org/10.1007/s005310050129, 1997.

Scott, D. and Thomsen, L. A.: Society of Petroleum Engineers SPE 25674 A Global Algorithm for Pore Pressure Prediction, the SPE Middle East Oil Technical Conference & Exhibition held in Bahrain, 3–6, 1993.

Steiner, U., Savvatis, A., Böhm, F., and Schubert, A.: Explorationsstrategie tiefer geothermischer Ressourcen am Beispiel des süddeutschen Oberjuras (Malm), in: Handbuch Tiefe Geothermie, edited by: Bauer, M., Freeden, W., Jacobi, H., and Neu, T., Springer Berlin Heidelberg, Berlin, Heidelberg, 429–462, 2014.

Suggate, R. P.: Relations between depth of burial, vitrinite reflectance and geothermal gradient, J. Petrol. Geol., 21, 5–32, 1998.

Sweeney, J. J. and Burnham, A. K.: Evaluation of a simple model of vitrinite reflectance based on chemical kinetics, Am. Assoc. Petrol. Geol. Bull., 74, 1559–1570, 1990.

Taylor, G. H., Teichmüller, M., Davis, A., Diessel, C. F. K., Littke, R., and Robert, P.: Organic petrology, Borntraeger, Berlin, Stuttgart, ISBN 978-3-443-01036-2, 1998.

Valečka, J., Skoček, V.: Late Cretaceous lithoevents in the Bohemian Cretaceous Basin, Czechoslovakia, Cretaceous Res., 12, 561–577, 1991.

Vamvaka, A., Siebel, W., Chen, F., and Rohrmüller, J.: Apatite fission-track dating and low-temperature history of the Bavarian Forest (southern Bohemian Massif), Int. J. Earth Sci., 103, 103–119, https://doi.org/10.1007/s00531-013-0945-x, 2014.

Vasseur, G., Djéran-Maigre, I., Grunberger, D., Rousset, G., Tessier, D., and Velde, B.: Evolution of structural and physical parameters of clays during experimental compaction, Mar. Petrol. Geol., 12, 941–954, 1995.

Voigt, S., Aurag, A., Leis, F., and Kaplan, U.: Late Cenomanian to Middle Turonian high-resolution carbon isotope stratigraphy: New data from the Münsterland Cretaceous Basin, Germany, Earth Planet. Sci. Lett., 253, 196–210, https://doi.org/10.1016/j.epsl.2006.10.026, 2007.

Voigt, S., Wagreich, M., Surlyk, F., Walaszczyk, I., Uličný, D., Čech, S., Voigt, T., Wiese, F., Wilmsen, M., Niebuhr, B., Reich, M., Funk, H., Michalík, J., Jagt, J. W. M., Felder, P. J., and Schulp, A. S.: Cretaceous, in: The Geology of Central Europe, Volume 2: Mesozoic and Cenozoic, edited by: McCann, T., Geol. Soc. Lond., 2, 923–998, 2008.

Voigt, T., Kley, J., and Voigt, S.: Dawn and dusk of Late Cretaceous basin inversion in central Europe, Solid Earth, 12, 1443–1471, https://doi.org/10.5194/se-12-1443-2021, 2021.

von Eynatten, H., Kley, J., Dunkl, I., Hoffmann, V.-E., and Simon, A.: Late Cretaceous to Paleogene exhumation in central Europe – localized inversion vs. large-scale domal uplift, Solid Earth, 12, 935–958, https://doi.org/10.5194/se-12-935-2021, 2021.

Von Freyberg, B.: Tektonische Karte der Fränkischen Alb und ihrer Umgebung, Erlanger Geol. Abh., 77, 1969.

Wagner, G. A., Coyle, D. A., Duyster, J., Henjes-Kunst, F., Peterek, A., Schröder, B., Stöckhert, B., Wemmer, K., Zulauf, G., Ahrendt, H., Bischoff, R., Hejl, E., Jacobs, J., Menzel, D., Lal, N., van den Haute, P., Vercoutere C., and Welzel, B.: Post-Variscan thermal and tectonic evolution of the KTB site and its surroundings, J. Geophys. Res., 102, 18221–18232, 1997.

Welz, H.: Sedimentologische, petrographische und geophysikalische Untersuchungen im Lias epsilon (Posidonienschiefer) der Nördlichen Frankenalb sowie eine wirtschaftsgeologische Bewertung eines ausgewählten Vorkommens, Friedrich-Alexander-Universität Erlangen-Nürnberg, Erlangen, [data set], 1994.

Yang, Y. and Aplin, A. C.: A method for the disaggregation of mudstones, Sedimentology, 44, 559–562, 1997.

Yang, Y. and Aplin, A. C.: Definition and practical application of mudstone porosity-effective stress relationship, Petrol. Geosci., 10, 153–162, 2004.

Ziegler, P. A.: Late Cretaceous and Cenozoic intra-plate compressional deformations in the Alpine foreland – a geodynamic model, Tectonophysics, 137, 389–420, 1987.

Zulauf, G.: Brittle deformation events at the western border of the Bohemian Massif (Germany), Geol. Rundsch., 82, 489–504, https://doi.org/10.1007/BF00212412, 1993.

Zweigel, J., Aigner, T., and Luterbacher, H. P.: Eustatic versus tectonic controls on Alpine foreland basin fill: sequence stratigraphy and subsidence analysis in the SE German Molasse, Geol. Soc. Lond., 134, 299–323, 1998.